

LA-UR-15-21843 (Accepted Manuscript)

Approximate models for the ion-kinetic regime in inertial-confinement-fusion capsule implosions

Hoffman, Nelson M.; Zimmerman, George B.; Molvig, Kim; Rinderknecht, Hans. G.; Rosenberg, Michael J.; Albright, Brian James; Simakov, Andrei Nikolaevich; Sio, Hong; Zylstra, Alex B.; Gatu Johnson, Maria; Seguin, Fredrick H.; Frenje, Johan A.; Li, Chikang; Petrasso, Richard D.; Higdon, David Mitchell; Srinivasan, Gowri; Glebov, Vladimir Yu.; Stoeckl, Christian; Seka, Wolf; Sangster, T. Craig

Provided by the author(s) and the Los Alamos National Laboratory (2015-10-29).

To be published in: Physics of Plasmas, Vol.22, iss.5, p.052707, May 2015.

DOI to publisher's version: 10.1063/1.4921130

Permalink to record: <http://permalink.lanl.gov/object/view?what=info:lanl-repo/lareport/LA-UR-15-21843>

Disclaimer:

Approved for public release. Los Alamos National Laboratory, an affirmative action/equal opportunity employer, is operated by the Los Alamos National Security, LLC for the National Nuclear Security Administration of the U.S. Department of Energy under contract DE-AC52-06NA25396. Los Alamos National Laboratory strongly supports academic freedom and a researcher's right to publish; as an institution, however, the Laboratory does not endorse the viewpoint of a publication or guarantee its technical correctness.

Approximate models for the ion-kinetic regime in inertial-confinement-fusion capsule implosions

Rev 5.2, 30 April 2015

Nelson M. Hoffman^{1†}, George B. Zimmerman², Kim Molvig¹, Hans G. Rinderknecht³, Michael J. Rosenberg³, B. J. Albright¹, Andrei N. Simakov¹, Hong Sio³, Alex B. Zylstra³, Maria Gatu Johnson³, Fredrick H. Séguin³, Johan A. Frenje³, C. K. Li³, Richard D. Petrasso³, David M. Higdon¹, Gowri Srinivasan¹, Vladimir Yu. Glebov⁴, Christian Stoeckl⁴, Wolf Seka⁴, T. Craig Sangster⁴

¹ Los Alamos National Laboratory, P. O. Box 1663, Los Alamos, New Mexico 87545, USA

² Lawrence Livermore National Laboratory, Livermore, California 94550, USA

³ Plasma Science and Fusion Center, Massachusetts Institute of Technology, Cambridge, Massachusetts 02139, USA

⁴ Laboratory for Laser Energetics, University of Rochester, Rochester, New York 14623, USA

†Corresponding author's email: nmh@lanl.gov

Abstract. “Reduced” (i.e., simplified or approximate) ion-kinetic (RIK) models in radiation-hydrodynamic simulations permit a useful description of inertial-confinement-fusion (ICF) implosions where kinetic deviations from hydrodynamic behavior are important. For implosions in or near the kinetic regime (i.e., when ion mean free paths are comparable to the capsule size), simulations using a RIK model give a detailed picture of the time- and space-dependent structure of imploding capsules, allow an assessment of the relative importance of various kinetic processes during the implosion, enable explanations of past and current observations, and permit predictions of the results of future experiments. The RIK simulation method described here uses moment-based reduced kinetic models for transport of mass, momentum, and energy by long-mean-free-path ions, a model for the decrease of fusion reactivity owing to the associated modification of the ion distribution function, and a model of hydrodynamic turbulent mixing. The transport models are based on local gradient-diffusion approximations for the transport of moments of the ion distribution functions, with coefficients to impose flux limiting or account for transport modification. After calibration against a reference set of ICF implosions spanning the hydrodynamic-to-kinetic transition, the method has useful, quantifiable predictive ability over a broad range of capsule parameter space. Calibrated RIK simulations show that an important contributor to ion species separation in ICF capsule implosions is the preferential flux of longer-mean-free-path species out of the fuel and into the shell, leaving the fuel relatively enriched in species with shorter mean free paths. Also,

the transport of ion thermal energy is enhanced in the kinetic regime, causing the fuel region to have a more uniform, lower ion temperature, extending over a larger volume, than implied by clean simulations. We expect that the success of our simple approach will motivate continued theoretical research into the development of first-principles-based, comprehensive, self-consistent, yet useable models of kinetic multispecies ion behavior in ICF plasmas.

I. Introduction

In a strongly driven inertial-confinement-fusion (ICF) capsule, the fuel may be heated to such high temperature that the mean free path of thermal ions ($\lambda_i \sim T^2 / Z_i^2 Z^2 \rho$ for ions of charge Z_i moving in a background plasma having ion temperature T , ion charge Z , and density ρ) becomes comparable to the size of the fuel region. In this case, the fuel cannot be adequately represented as a hydrodynamic fluid (i.e., an aggregation of particles such that, owing to high collision rates, all constituent particles have Maxwellian velocity distributions characterized by a local temperature) but must instead be treated as a kinetic plasma, whose velocity distribution function requires a full phase-space description. Even in less extreme situations, the mean free paths of those energetic ions responsible for most fusion reactions and for the transport of mass, momentum, and energy in the capsule's core can be so long that a non-local description of transport is required.

Several authors have commented from a theoretical standpoint on the possible role of kinetic phenomena and the need to account for them in simulations of ICF implosions^{1,2,3,4,5,6,7,8,9,10}. Recently, a variety of implosion experiments has given strong evidence for the importance of ion-kinetic transport in the ICF context^{11,12,13,14,15}. In our earlier work, we described a simplified asymptotic model for the reduction of fusion reactivity in ICF capsules⁴, owing to the depletion of the tail of the ion distribution function near the “Gamow peak”, where most fusion reactions occur. The model was implemented in a radiation-

hydrodynamic simulation code, and, when augmented with a model of hydrodynamic turbulent mixing, was used successfully to explain the observed behavior of a diverse set of DT-filled plastic-shell capsules.¹⁶ The model did not, however, account in a unified framework for the modified transport of mass, momentum, and energy associated with kinetic departures from local Maxwellian behavior. Instead, kinetic mass transport was represented approximately by the depletion of the distribution tail without normalization, enhancing the reduction in fusion reactivity. The article by Albright *et al.*⁵ describes improvements to this approach., which we summarize in Sec. II.E.

In the present article we report on a simulation and prediction method using models of kinetically modified mass, momentum, and energy transport in ICF implosions, as well as the improved reactivity-reduction (“Knudsen-layer reactivity”) model. The combination of these models, in a standard sequential operator-split approach, allows more comprehensive simulations of strongly kinetic ICF implosions, extending to those in which the fuel-averaged Knudsen number N_K , defined as the ratio of thermal ion mean free path to fuel region size, is ≥ 1 at “bang time” (the time of peak fusion reaction rate). The models are implemented in a Lagrangian radiation-hydrodynamics code, which also incorporates multigroup thermal radiation diffusion, transport of charged fusion-product particles, artificial viscosity, realistic equations-of-state with detailed ionization physics, non-LTE opacities, laser propagation via geometric ray tracing, and laser deposition by inverse bremsstrahlung. Electron thermal transport is treated using flux-limited thermal diffusion, with a flux limiter $f_e = 0.06$. Since we neglect non-local electron thermal transport, we restrict attention to direct-drive ICF capsules imploded by square pulses of 1 ns duration or shorter, where it has been shown that flux-limited electron thermal diffusion using $f_e = 0.06$ allows an adequate description of the mean flow of the system.^{17,18} All implosion simulations assume 1D spherical symmetry, a good approximation for the low-convergence capsules discussed in this article.

The simulation code does not include models of stimulated laser-matter interaction processes such as stimulated Brillouin scattering, two-plasmon decay, or cross-beam energy transfer. Furthermore, although laser energy is propagated and deposited using geometric rays, the true laser illumination pattern cannot be accurately represented in 1D implosion simulations. For these reasons, the total energy E_L of the laser pulse in an implosion experiment is not introduced into a simulation; instead, a smaller amount of energy $f_{is}E_L$ is introduced, where the laser source fraction $f_{is} < 1$. The missing energy $(1 - f_{is})E_L$ corresponds to the laser energy scattered and refracted away from the capsule by unmodeled stimulated processes and unmodeled 3D ray geometry effects, respectively, in the experiment. The fraction of total energy E_L absorbed by the capsule in simulations, $f_{abs,sim}$, is always less than f_{is} , because the simulation does attempt to account for the refraction of laser light passing the capsule without being absorbed. If we denote the amount of such refracted unabsorbed energy in the simulation by $f_{refrac,sim}E_L$, then $f_{abs,sim} = f_{is} - f_{refrac,sim} < f_{is}$. We regard f_{is} as a simulation parameter to be calibrated using data from experiments; it is not a measureable quantity, but measurements of the absorbed energy fraction f_{abs} are important in constraining its value¹⁹.

We refer to the combination of models described in this article as the overall *reduced* (in the sense of simplified and approximate) *ion-kinetic*, or *RIK, model*. In Sec. II, we describe the individual component models making up the full RIK model. For completeness we also include in our method a model of hydrodynamic turbulent mixing. This phenomenon is not a kinetic effect at all, but it is traditionally considered to play a strong role in ICF implosions, and we need a way to assess its effects relative to those of ion-kinetic phenomena; this model is also described in Sec. II. In Sec. III we discuss our methodology for calibrating parameters of the component models, the various sets of ICF capsule experiments used for calibrations (a set that is significantly more diverse than even those experiments used in Ref. 4), the results of the calibration process, and progress in the validation of the calibrated models. In Sec. III we also

point out that, according to RIK simulations, ion-kinetic transport can extensively modify the structure of imploding capsules, producing a differential loss of fuel ions into the imploding shell and a large ion-heated region in fuel and shell. Section IV summarizes our findings and conclusions.

II. Component models included in the RIK method

A. The approximate nature of the RIK model

It is important to begin with a caveat: the RIK model introduced here must be regarded as provisional or *schematic*. In other words, it is an outline or “rough draft” of a rigorous model, good enough for making predictions and gaining insight, but not in any way a finished theoretical picture. Its approximations and assumptions that limit any claims to rigor will be clearly highlighted, and the shortcomings in its explanatory and predictive power will become obvious. Yet the RIK model’s successes, as we report here, have made it a tool of significant utility, and we believe it to be an important milestone on the path to a rigorous model. We expect that whatever success it has achieved will stimulate continued theoretical developments in that direction; some recent progress along that line will be noted below.

Among other approximations, the RIK model uses a set of gradient-diffusion models implemented in the host radiation-hydrodynamics code. Clearly, local-gradient-driven processes are not justifiable as one approaches the limit of increasingly long ion mean free path and non-locality of the transport processes. Therefore, some of the component models in the RIK model incorporate a flux limiter, whose purpose is to allow a bridging between the short mean-free-path hydrodynamic regime and the long mean-free-path kinetic regime.²⁰ In the present work, we report results based on using flux limiters that are specified either *a priori* or as a result of empirical calibration. A further major approximation is that the parameters of each component model are permitted to vary independently of the parameters in any other

component model. The expectation is that systematic correlations among parameters of different component models, while they might have been specified *a priori* by an overarching theory, will be revealed through empirical calibration, given enough data; in fact, exactly such correlated behavior does emerge from our methodology, as we will show below. Other important approximations relate to the ion mass transport model, as we now describe.

B. Multispecies ion mass transport

The starting point for the RIK ion mass transport technique is the multispecies model discussed by Schunk²¹, with modifications by Zimmerman²². We refer to the resulting method, together with the ion enthalpy transport, frictional heating, viscosity, and thermal conductivity models discussed below, as the Schunk-Zimmerman model. Its particular form is based on Schunk's 8-moment approximation²³. Schunk's model is an attempt to describe plasmas that are far from equilibrium, in the manner of Grad²⁴; his goal was a model that could apply to plasmas with large temperature and drift velocity differences among the interacting species. As a result, the model employs approximate velocity distribution functions that prevent it from reaching the Chapman-Enskog limit in highly collisional situations. Given the heuristic nature of some of Schunk's approximations, it is not clear how widely valid the model can be. A detailed comparison to a more rigorous theory such as the generalized Chapman-Enskog method of Molvig, Simakov, and Vold applied to a binary-mixture plasma²⁵ will be required for revealing the extent to which the Schunk model is accurate in various regimes. Another consequence of the 8-moment approximation is the neglect of temperature and pressure anisotropy. For imploding shock waves in ICF capsules, temperature anisotropy may occur; an example is displayed in the Vlasov-Fokker-Planck implosion simulations by Larroche [Ref. 2]. It is not clear whether this phenomenon leads to observable effects in current experimental observations. But in any case it cannot be represented in the Schunk-Zimmerman model, and could not be treated

straightforwardly in the kind of standard radiation-hydrodynamics code used in our work. Properly accounting for temperature and pressure anisotropy therefore remains, for now, a topic for future investigation.

The Schunk-Zimmerman model involves a heuristic treatment of the collisional frictional force on each species. One fundamental approximation is that the model regards the frictional drag on each species as occurring against the average background plasma, rather than considering other species separately in pairwise fashion. Schunk's frictional momentum exchange term for ion species s (with units, for example, $\text{g cm}^{-2} \text{s}^{-2}$, i.e., unit momentum per unit volume per unit time) can be written

$$\sum_j n_s n_j R_{sj} (\vec{w}_j - \vec{w}_s),$$

where the sum extends over all species j , n_j is the density of species j , \vec{w}_j is the diffusion velocity of species j relative to the mass-averaged velocity of the plasma (represented by the zone velocity in the simulation code), and R_{sj} (with units, e.g., $\text{g cm}^3 \text{s}^{-1}$) gives the rate of momentum exchange.²⁶ In the Schunk-Zimmerman model, Schunk's expression is replaced with

$$-\vec{w}_s \frac{n_s m_s}{\tau_s},$$

where τ_s is an average collision time between species s and all other species. When there are three or more species present, as is often the case in problems of practical interest, the collision time is given by

$$\tau_s = \frac{3}{4\sqrt{2}\pi} \frac{m_p^{1/2} T_i^{3/2}}{e^4 \ln \Lambda} \sqrt{\frac{1}{\bar{A}} + \frac{1}{A_s}} \frac{A_s}{Z_s^2 \sum_j n_j Z_j^2}, \quad (1)$$

where species j has mass number A_j and charge state Z_j , and \bar{A} is the molar-average mass. This expression is obtained from Schunk's Eq. C2 for the pairwise collision frequency ν_{st} . We define a total collision frequency for species s as the sum of ν_{st} over all species t , with the assumption of

a single temperature and Coulomb logarithm for all pairs of species, and define a mean reduced mass number $\sqrt{\frac{1}{A} + \frac{1}{A_s}}$ for species s . The collision time in Eq. 1 is the reciprocal of the total collision frequency.

A second important approximation in the Schunk-Zimmerman model is that the thermal diffusive force resulting from the ion temperature gradient is omitted. The omission is largely a practical decision, as this term's proper treatment would present serious complications. As pointed out by various authors, the thermodiffusion coefficients are not thermodynamic properties of an equilibrium plasma, but depend significantly on the interparticle potential or “the law governing the molecular interactions”²⁷, necessitating a kinetic evaluation²⁸. This approximation is justifiable in situations where the ion temperature gradient $\nabla T_i/T_i$ is small and transient compared to other gradients, such as the concentration gradient $\nabla P_s/P_s$, which is usually large and persistent locally at material boundaries.²⁹ We can also expect this approximation to be useful when $T_i \approx T_e$, since then the electron thermodiffusion term, which is explicitly represented in the expression for ion mass flux (Eq. 2 below), can account for ion thermodiffusion as well, with a properly calibrated multiplier.

A third major approximation, or limitation, of the Schunk-Zimmerman model as invoked in this work is that it does not currently incorporate flux limiters in its expression for ion mass flux. Since the expression includes terms representing several gradient-based forces, each of which might need its own independent flux limiter, the introduction of flux limiters here would spawn a proliferation of adjustable parameters, and a degree of complexity even beyond the already considerable level the model now has. Furthermore, given the severe approximations the model incorporates, the addition of flux limiters to each gradient-driven term seems like an unwarranted refinement. As discussed below, we will apply a single multiplier to the ion mass flux to play the role of a flux limiter, if necessary.

Other simplifications used in the Schunk-Zimmerman model include the neglect of time derivatives of \vec{w}_s and species heat fluxes \vec{q}_s , terms proportional to $\vec{w}_s \cdot \vec{q}_s$, and magnetic fields. Again these approximations have consequences primarily for the structure of shock waves, and we will depend on empirically calibrated multipliers to compensate for errors they may induce. The model assumes zero net charge density, and that all ion species have the same temperature.

Using Schunk's Eq. 27b, with his Eq. 25b for the collision term, and our approximations above, the mass flux of ion species s , relative to the mass-weighted background of all species, is written as

$$m_s \hat{\mathcal{F}}_s \equiv m_s n_s w_s = \tau_s \left\{ \begin{aligned} & -\nabla P_s + \frac{n_s A_s}{\sum_j n_j A_j} \nabla \sum_j P_j - \left(\frac{n_s Z_s}{\sum_j n_j Z_j} - \frac{n_s A_s}{\sum_j n_j A_j} \right) \nabla P_e \\ & + f_{Te} \beta_{\parallel}^{uT} \left(\frac{n_s Z_s^2}{\sum_j n_j Z_j^2} - \frac{n_s Z_s}{\sum_j n_j Z_j} \right) \nabla T_e \end{aligned} \right\}, \quad (2)$$

where

$$\beta_{\parallel}^{uT} = n_e \frac{3}{2} \frac{\bar{Z} + 0.477}{\bar{Z} + 2.15}, \text{ with } \bar{Z} \equiv \frac{\langle Z^2 \rangle}{\langle Z \rangle}.$$

Time derivatives are neglected in Schunk's expressions, as are body forces other than the electric field, which is replaced using the analogous electron momentum equation assuming zero net current. Thus here the term in ∇P_e incorporates the effect of the ambipolar electric field. The expression for β_{\parallel}^{uT} is based on a fit to β_0 in Table 2 of Braginskii³⁰. The multiplier f_{Te} controls the contribution of the ∇T_e term, and is a parameter to be experimentally calibrated. The first two terms in the bracket correspond exactly to the first two terms of Zel'dovich and Raizer for species mass flux in a neutral binary fluid (with $P_e = 0$, $Z_j = 0$).²⁷

The benefit of the Schunk-Zimmerman model is that it allows a simple evaluation of τ_s and the ion species flux $\hat{\mathcal{F}}_s$ for all species, even when a very large number of species is present. It

gives a reasonable approximation to the mass flux of species that have low mass density relative to the entire plasma, while underestimating the flux of the species with highest mass density. Since the highest density species, by definition, do not diffuse significantly with respect to the mass (i.e., density)-averaged velocity of the plasma, this underestimate does not introduce major inaccuracies; it is usually most important to have an accurate model of the low-density species, which typically are the most mobile. The model may underestimate the degree to which two minority high-Z species relax towards each other rather than the low-Z species. If the high-Z species constitute a small mass fraction of the plasma, the high-Z species' mean velocity could be persistently different than the mass-averaged plasma velocity. Generally, however, we do not expect this limitation to induce major errors in simulations where low-Z and high-Z species are initially separated (as in an ICF capsule), since only a small volume of the system is likely to be affected. Another consequence of this approximation is that the mass-averaged sum of the species diffusion velocities $\sum_j n_j m_j \bar{w}_j$ does not vanish. This means that the mesh zone boundaries become arbitrary divisions of the system geometry, while mass conservation is assured by accounting for species fluxes across zone boundaries, as is routinely done for simulations that depart from a purely Lagrangian approach .

Associated with mass transport is a corresponding energy transport resulting from the ions' enthalpy. The ions carry their own thermal energy with them as they flow, and the divergence of this flux causes heating that must be accounted for in the model. There is also frictional heating resulting from momentum exchange among species. These processes are a component of energy transport that is distinct from ion thermal conduction, which occurs independently of any interspecies mass flux.

In the Schunk-Zimmerman model, since the collisional momentum-exchange term is approximated as

$$\sum_j n_s n_j R_{sj} (\vec{w}_j - \vec{w}_s) \cong -\vec{w}_s \frac{n_s m_s}{\tau_s} = -\frac{m_s \hat{\mathcal{F}}_s}{\tau_s}, \quad (3)$$

we find the ion heating rate resulting from the relative motion of ion species to be

$$\hat{Q}_{ion} = \sum_s \frac{m_s \hat{\mathcal{F}}_s}{\tau_s} \vec{w}_s - \frac{3}{2} \vec{\nabla} \cdot (T_i \sum_s \vec{w}_s n_s) - \sum_s P_s \vec{\nabla} \cdot \vec{w}_s, \quad (4)$$

with units energy per unit volume per unit time. The first term describes frictional heating;

every member of the sum is positive definite, since $\vec{w}_s \equiv \hat{\mathcal{F}}_s / n_s$ has the same sign as $\hat{\mathcal{F}}_s$. Thus

the term is always positive, a necessary property of frictional heating. The second term

describes the divergence of the thermal energy flux. The third term represents a correction to

the PdV work term in the momentum equation for the mean flow, since the mean flow

equations do not account for interspecies diffusion.

The analogous electron heating rate resulting from the ions' relative motion is

$$\hat{Q}_{ele} = -\frac{3}{2} \vec{\nabla} \cdot \vec{w}_e T_e n_e - P_e \vec{\nabla} \cdot \vec{w}_e - T_e \vec{\nabla} \cdot [(\vec{w}_e - \vec{w}_{z2}) \beta_0 n_e],$$

with the definitions

$$\vec{w}_e \equiv \frac{\sum_j n_j Z_j \vec{w}_j}{\sum_j n_j Z_j} \text{ and } \vec{w}_{z2} \equiv \frac{\sum_j n_j Z_j^2 \vec{w}_j}{\sum_j n_j Z_j^2}.$$

The final term includes $\vec{E} \cdot \vec{J}$ where \vec{E} is the thermoelectric field and \vec{J} is the current associated with \vec{w}_e .

Since the model as implemented is not flux-limited, Eq. 2 may give values of $m_s \hat{\mathcal{F}}_s$ that are larger than is physically possible in regions where the gradients are very steep. Because of this, and the other approximations noted above, we introduce another empirically calibrated multiplier f_{dif} , whose value is determined by requiring simulations to conform to observations, and implement the species mass flux as

$$m_s \mathcal{F}_s = f_{dif} m_s \hat{\mathcal{F}}_s. \quad (5)$$

If we find, for example, that the empirically inferred value of f_{dif} is smaller than unity for a particular capsule implosion, that may be evidence that the implosion enters the ion-kinetic regime where ion mean free paths are larger than local gradient scale lengths, so f_{dif} acts as an empirically determined flux limiter. Alternatively, it may be that the sign of the missing ion-thermodiffusion term is such as to reduce the species flux, so $f_{dif} < 1$ is necessary to express the effect of the missing term. In the same spirit we introduce the parameter f_{iht} to control the strength of the ion and electron heating rates: $Q_{ion} = f_{iht} \hat{Q}_{ion}$ and $Q_{ele} = f_{iht} \hat{Q}_{ele}$, and calibrate it empirically.

C. Ion viscosity (momentum transport)

In the absence of a magnetic field, the ion viscosity is^{22,31}

$$\eta_i = f_{ivis} \times 0.96 \frac{3}{4\sqrt{\pi}} \frac{m_u^{1/2} T_i^{5/2}}{e^4 \ln \Lambda} \frac{\langle A^{1/2} / Z^2 \rangle}{\langle Z^2 \rangle}, \quad (6)$$

where m_u is the atomic mass unit. The ion viscosity is added to the artificial viscosity, whose value is set to maintain shock wave widths of at least two mesh cells. The multiplier f_{ivis} is a parameter to be experimentally calibrated.

D. Ion thermal conduction

Thermal conduction by ions is represented with a flux-limited gradient-diffusion model:

$$q_i = f_{icnd} \min \left(\kappa_i \nabla T_i, \frac{q_{i,stream}}{f_{glcm}} \right) = \frac{f_{icnd} \kappa_i \nabla T_i}{\max \left(1, f_{glcm} \frac{\kappa_i |\nabla T_i|}{q_{i,stream}} \right)},$$

where q_i is the conductive heat flux carried by ions, κ_i is the local Spitzer-Härm ion-thermal conductivity:

$$\kappa_i = 3.9 \frac{n_i T_i}{\langle m_i \rangle} \tau_u \propto \frac{n_i T_i}{m_u} \frac{m_u^{1/2} T_i^{3/2}}{n_i \ln \Lambda} \frac{\langle \frac{1}{A^{1/2} Z^2} \rangle}{\langle Z^2 \rangle} \propto \frac{T_i^{5/2}}{m_u^{1/2} \ln \Lambda} \frac{\langle \frac{1}{A^{1/2} Z^2} \rangle}{\langle Z^2 \rangle}.$$

T_i and n_i are the local ion temperature and total ion number density, respectively, in the underlying radiation-hydrodynamic code, $q_{i,stream}$ is the heat flux in the streaming limit

$$q_{i,stream} \propto \frac{n_i T_i^{3/2}}{m_u^{1/2}} \left\langle \frac{1}{A^{1/2}} \right\rangle,$$

f_{iflxm} is a flux-limit parameter, and f_{icnd} is a coefficient to be empirically calibrated. The form of the flux limiter is specified *a priori* here, although it contains the parameter f_{iflxm} that can be constrained empirically if desired; in practice $f_{iflxm} = 1$ for all models discussed in this article.

E. Fusion reactivity reduction

The fusion-reactivity reduction model (“Knudsen reactivity”) is an improved version of the asymptotic model published in Molvig *et al.*⁴ to describe the decrease in fusion reactivity resulting from the escape of long-mean-free-path ions from a small volume of fuel. The new model⁵, which we refer to as “Knudsen II” or the Molvig-Albright reactivity reduction model, uses an accurate solution to the loss-term kinetic equation, described in Ref. 4 for the ion distribution function $f_i(\varepsilon)$,

$$\frac{\partial}{\partial \varepsilon} \left[f_i + \frac{\partial}{\partial \varepsilon} f_i \right] - N_{Ki}^2 \varepsilon^3 f_i = 0, \quad (7)$$

rather than the leading-order WKB solution; here $\varepsilon \equiv m_i v^2 / 2kT_i$, where v is the ion velocity, and N_{Ki} is the Knudsen number for species i (defined below). The Molvig-Albright model uses distinct distribution functions (assumed to be isotropic) for the reacting species. The distribution functions are normalized, so that the model accounts only for the modified shape of the high-energy tail of the distribution function, not the loss of the ions from the fuel volume; the latter effect is now represented by the multispecies ion-mass-transport model described

earlier. As in Ref. 4, Bosch-Hale cross-sections³² are used in the evaluation of fusion reactivities.

The full 3D velocity-space integral, appropriate for non-Maxwellian distributions, is used to evaluate reactivity. For two reacting species with mass numbers and distribution functions $A_1, f_1(\varepsilon_1)$ and $A_2, f_2(\varepsilon_2)$, respectively, the fusion reactivity in $\text{cm}^3 \text{s}^{-1}$ is

$$\langle \sigma v \rangle_{12} = 3.096 \times 10^{-17} T^{1/2} \frac{2\sqrt{2}}{\pi} \sqrt{\frac{A_1 + A_2}{A_1 A_2}} \int_0^\infty \varepsilon_1^{1/2} f_1(\varepsilon_1) \int_0^\infty \varepsilon_2^{1/2} f_2(\varepsilon_2) \int_{-1}^{+1} v_r(\xi, \varepsilon_1, \varepsilon_2) \sigma(v_r^2 T) d\xi d\varepsilon_1 d\varepsilon_2$$

where T has units keV, σ is in barns, and v_r is the relative velocity of the two reacting nuclei, which depends on the angle ξ between their respective velocities:

$$v_r(\xi, \varepsilon_1, \varepsilon_2) \equiv \sqrt{\frac{A_2}{A_1 + A_2} \varepsilon_1 + \frac{A_1}{A_1 + A_2} \varepsilon_2 - 2\xi \frac{\sqrt{A_1 A_2}}{A_1 + A_2} \varepsilon_1^{1/2} \varepsilon_2^{1/2}}.$$

In the reactivity-reduction model, the local Knudsen number is defined as

$$\begin{aligned} N_{Ki} &\equiv \frac{\lambda_i}{L} = f_{Knu} \frac{m_p}{\pi \sqrt{3} e^4} \frac{1}{Z_i^2 A_i^{1/2}} \frac{\sum_j n_j A_j}{\sqrt{\sum_j n_j Z_j^2 \sum_j n_j Z_j^2 / A_j}} \frac{T_i^2}{\ln \Lambda \rho L} \\ &\cong 1.4825 \times 10^{-5} \frac{f_{Knu}}{Z_i^2 A_i^{1/2}} \frac{\sum_j n_j A_j}{\sqrt{\sum_j n_j Z_j^2 \sum_j n_j Z_j^2 / A_j}} \frac{T_i^2}{\ln \Lambda \rho L} \end{aligned} \quad (8)$$

for ions with mass number A_i , charge Z_i , interacting with a background plasma of mass density ρ , Coulomb logarithm $\ln \Lambda$, consisting of a mixture of ion species j , each characterized by mass number A_j , charge Z_j , and number density n_j . The symbol λ_i denotes the mean free path of thermal ions i , and L denotes the size of the system. The coefficient f_{Knu} may be regarded as compensating for approximations in the loss-term kinetic equation (Eq. 7) and in the definition of L , and is to be empirically calibrated.

In Eq. 8, T_i , ρ , and L have units keV, g/cm³, and cm respectively. Writing $N_{Ki} = C \frac{4}{\ln \Lambda} \frac{T_i^2}{\rho L}$,

where L now has units of μm , and setting f_{Knu} to 1, we find for example that $C = 0.043$ for deuterons in a 50/50 D³He mixture, $C = 0.009$ for ³He in that mixture, and $C = 0.091$ for a fictitious particle with $A=2.5$ and $Z=1$ in a 50/50 DT mixture. We usually characterize the background plasma by its proton Knudsen number N_{Kp} , using $A=1$ and $Z=1$. The Knudsen number for a different particle i is then $N_{Ki} = N_{Kp}/Z_i^2 A_i^{1/2}$.

As in Ref. 4, we typically calculate the system size L locally as the inverse of a root-mean-square reciprocal distance to the boundary of the spherical reacting volume, normalized such that in plane geometry the result limits to the distance to the boundary. The boundary is defined as the radial point at which the fusion reaction rate has dropped to some fraction (usually 0.001) of its maximum value; this definition is useful no matter whether the boundary is sharp, diffuse, or if reactions are occurring primarily in a shock wave far from a material interface. Alternative definitions of L have been investigated; for example, we can define L as the local ion-temperature curvature scale length: $L \equiv \sqrt{-T_i/\nabla^2 T_i}$. Another option is to employ a flux-limited version of the loss-term kinetic equation, which generally reduces the amount of tail depletion, and hence reduces the effect of tail depletion on fusion reactivity.

For a given fusion reaction, Eq. 7 is solved for various values of N_{Ki} for each reacting species, and the resulting distribution functions used to compute a table of mean reactivity $\langle \sigma v \rangle$ as a function of T_i and N_{Kp} . In implosion simulations, the reactivity is determined in each cell and each timestep by interpolating in the table, given the cell's local T_i and N_{Kp} . Figure 1 shows the fusion reactivity reduction ratio $\langle \sigma v \rangle(T_i, N_{Kp})/\langle \sigma v \rangle(T_i, 0)$ for DDn and D³He reactions. For D³He, the “reduction ratio” actually becomes an enhancement in the reactivity at very high ion temperature ($> \sim 300$ keV). In such cases, tail-ion loss and normalization cause a shift of the distribution downward in energy, giving greater overlap with the resonance in the D³He cross

section. A similar feature is seen for the DT reaction, but not for the DD reaction, which has no resonance.

F. Hydrodynamic turbulent mixing

Turbulent mixing is represented by the buoyancy-drag model of Dimonte³³. The model has two main parameters, a drag coefficient and an initial scale length l . Two coupled equations describe the evolution of the bubble height (i.e., the penetration of the low-density fluid into the high-density fluid) and the spike length (i.e., the penetration of the high-density fluid into the low-density fluid) respectively. The drag coefficient has been independently determined to be equal to 2.5, and is set to that value for the results reported here. The initial scale length l is related to both the mean amplitude and mean transverse scale length of surface perturbations on the capsule, which may result from the initial surface roughness, or from laser imprint, or some other source. We regard l as a parameter to be inferred from the measurements.

III. Calibration and (in)validation of RIK models

A. Methodology

The full RIK model is a simultaneous implementation of the Schunk-Zimmerman ion transport model, the Molvig-Albright reactivity reduction model, and the Dimonte hydrodynamic turbulent mix model. To judge the explanatory and predictive value of the class of all RIK models, we have performed a calibration/(in)validation cycle^{34, 35} by using one set of experiments to calibrate model parameters, and then following the calibration process with an assessment [“(in)validation”] of the ability of the calibrated model to explain observations from other, independent experiments. We use the term “invalidation” as a reminder that, just as a physical theory can never be proven to be universally true, neither can a model be proven

generally valid in all regimes; a model can be either invalidated or “not yet invalidated”, and then typically only in a limited regime.

The calibration task is the optimization process of finding the RIK model that, when used in numerical simulations, gives the best explanation of the observations from one or more capsule implosion experiments. For a particular implosion, in principle the task entails searching a high-dimensional parameter space, the space of all possible RIK models (i.e., the RIK model *class*), where each model is characterized by the values of its various parameters, which were introduced in Secs. I and II. But in practice we have found useful models occupying a small volume of the entire model space; in fact, all the RIK models we discuss in the remainder of this article occupy a space of just two dimensions, spanned by the parameters f_{idif} and f_{icnd} . The other parameters (f_{ls} , f_e , f_{knu} , f_{iflxm} , f_{ivis} , f_{iht} , f_{Te} , and I) have fixed values for these RIK models, and four of those parameters are fixed at the value of zero.

The simulation code with its implementation of the RIK model class is essentially an operator, taking the model parameters as inputs and mapping them onto the output quantities characterizing the implosion, such as DT neutron yield Y_{DT} , DD neutron yield Y_{DDn} , D³He proton yield Y_{D^3He} , average ion temperature determined from DD neutron spectral width T_{iDD} , “bang time” t_b (the time of peak DD reaction rate in this article), absorbed laser energy E_{abs} (or, equivalently, absorbed laser fraction $f_{abs} \equiv E_{abs}/E_L$), and average shell areal density ρR_s . The goal is to find the model, i.e., the values of the input parameters, which minimizes the difference between the observed and simulated values of output quantities. We cast this as the least-squares problem of minimizing the sum S_N of squared differences between the observed and simulated values of N output quantities Q_j

$$S_N(\vec{f}) \equiv \sum_{j=1}^N \frac{[Q_{j,obs} - Q_{j,sim}(\vec{f})]^2}{\sigma_j^2}, \quad (9)$$

where the Q_j are Y_{DD} , T_{iDD} , t_b , etc., and σ_j denotes the uncertainty in the numerator, including the experimental uncertainty in $Q_{j,obs}$ as well as the simulation uncertainty in $Q_{j,sim}$. This expression shows explicitly the dependence of S_N and $Q_{j,sim}$ on the vector \vec{f} of model input parameters.³⁶ (In general, σ_j might also depend on \vec{f} , but we ignore that possibility for now.)

Searches of input parameter space are carried out using control scripts that automatically execute hundreds of 1D simulations in parallel, where each individual simulation has a unique set of input parameters. Typically only two input parameters are varied in any one search, so a comprehensive search of multidimensional input space requires searching numerous 2D slices. For each simulation, the sum S_N is evaluated, and the point in input space where S_N is minimized is identified. (Usually this is a unique point, but there is no guarantee that it is a global minimum.) We consider $D_N \equiv \sqrt{S_N} < \sqrt{N}$ to indicate a good fit of simulated outputs to observed outputs, since it means that $Q_{j,obs}$ matches $Q_{j,sim}$ to better than $1\sigma_j$ on average for all N output quantities.

Figure 2 shows a plot of $1/D_5$ on a 2D projection of input space with axes f_{dif} and f_{icnd} , for an OMEGA capsule implosion experiment in which five quantities were measured: Y_{DDn} , Y_{D^3He} , T_{iDD} , t_b , and f_{abs} . The plot represents the results of 120 1D simulations in which f_{dif} ranged over twelve values between 0 and 8 while f_{icnd} ranged over ten values between 0.2 and 20; thus only a small subset of points in the full parameter space is searched, but with appropriate conditions on the smoothness of D_5 , the sample is representative. The other eight input parameters were held fixed at $f_{is} = 0.63$, $f_e = 0.06$, $f_{Knu} = 0.1$, $f_{iflxm} = 1$, $f_{ivis} = f_{iht} = f_{Te} = l = 0$. The uncertainties appearing in the denominator of Eq. 9 were taken to be $\sigma_{YDD} = 10\%$, $\sigma_{YD^3He} = 10\%$, $\sigma_{TiDD} = 2$ keV, $\sigma_{tb} = 50$ ps, and $\sigma_{fabs} = 0.04$. The result of the study was that $\min(D_5) = 2.53$ (slightly larger than $\sqrt{5} = 2.24$), corresponding to input parameters $f_{dif} = 0.8$ and $f_{icnd} = 1.0$.

B. Calibration of RIK models

Our first attempt to calibrate RIK models used data from implosion experiments performed by Rosenberg *et al.*¹³ that were intended to span the range from hydrodynamic to kinetic behavior. The capsules had thin glass shells and were filled with equimolar D³He gas with initial densities in the range 0.14 to 3.1 mg/cm³. The implosions were driven by a 0.6-ns square laser pulse delivering ~14.6 kJ to the capsule. Detailed parameters describing eight of the capsules and their observed performance are given in Table I. Five measured quantities are shown for each capsule: Y_{DDn} , Y_{D^3He} , T_{iDD} , t_b , and f_{abs} . This is the data set used for calibration. Uncertainties in the measured quantities were given in the last paragraph of Sec. III. A.

Searches of input parameter space, as described in Sec. III. A, were carried out independently for each of the eight capsules, to find the RIK model that best described each capsule's behavior. It was determined early in the study that reasonably good fits could be obtained for all capsules by fixing eight of the ten input parameters at the values $f_{ls} = 0.63$, $f_e = 0.06$, $f_{Knu} = 0.1$, $f_{iflxm} = 1$, $f_{ivis} = f_{iht} = f_{Te} = l = 0$. This was true even though a wide range of values for f_{ls} , f_e , f_{Knu} , f_{iflxm} , f_{ivis} , and l was searched initially, for at least some capsules. Most of the final, more refined searches were therefore carried out in the $[f_{idif}, f_{icnd}]$ plane, for all capsules. The grid of interrogated points in the $[f_{idif}, f_{icnd}]$ plane consisted of the 120 ordered pairs having $f_{idif} \in [0.0, 0.1, 0.2, 0.3, 0.5, 0.8, 1.0, 2.0, 3.0, 4.0, 6.0, 8.0]$ and $f_{icnd} \in [0.2, 0.5, 1.0, 2.0, 4.0, 6.0, 8.0, 10.0, 15.0, 20.0]$. Resulting best-fit values for f_{idif} and f_{icnd} identified by the optimization process are given in Table II, where the capsules are arranged in order of decreasing initial fuel density (column 4). These optimal points must be members of the set of 120 discrete points just described.³⁷ The best-fit values for f_{idif} and f_{icnd} are also displayed as functions of initial fuel density in Figure 3.

Table II and Fig. 3 reveal an apparent continuous variation in the capsules' behavior as the initial fuel density is varied, as evidenced by the variation in the RIK models required to describe them. At the extremes, capsules with high initial fuel density > 2 mg/cm³ require $f_{idif} \cong$

$f_{icnd} \cong 1$, while capsules with low initial fuel density $< 1.2 \text{ mg/cm}^3$ require $f_{idif} \cong 0.1$ and $f_{icnd} = 4$ to 15. The variation is indicative of the distinction noted by Rosenberg *et al.*¹³ between capsules with fuel density $> 1.7 \text{ mg/cm}^3$, whose behavior they termed “hydrodynamiclike”, and those with fuel density $< 1.7 \text{ mg/cm}^3$, whose behavior they designated as “strongly kinetic.” In the strongly kinetic regime, yields are significantly smaller than predicted by “clean” hydrodynamic simulations (i.e., simulations having $f_{Knu} = 0$, $f_{idif} = 0$, $l = 0$, and $f_{icnd} = 1$, while all other parameters, except for f_{is} and f_e , are also 0).

The fact that $f_{idif} \cong f_{icnd} \cong 1$ for the high-fuel-density capsules shows that these quasi-hydrodynamic capsules are described fairly well by unmodified ion transport models, with no need for multipliers much different from unity. Yields of these capsules agree within a factor of about two with clean simulations, indicating that ion diffusion is of only moderate importance, since their calculated yields are somewhat insensitive to f_{idif} in the range $0 \leq f_{idif} \leq 1$. For the low-fuel-density capsules, on the other hand, our conclusion that $f_{idif} \cong 0.1$ is evidence that they evolve into the strongly kinetic regime where ion mean free paths exceed gradient scale lengths, so f_{idif} acts as a flux limiter. The small value of $f_{Knu} = 0.1$ for all these models indicates that the reactivity-reduction model, as invoked in this work, tends to overestimate the magnitude of the decrease in fusion reactivity caused by non-Maxwellian distributions. As mentioned earlier, this could result from the approximate definition of system size L or from the lack of a flux limiter in Eq. 7. A variety of other approximations is available in the implemented reactivity-reduction model, and will be investigated in future work.

Table II and Fig. 3 show a clear correlation between f_{idif} and f_{icnd} . This relationship illustrates what we expected we might see when making the approximation of *a priori* independence of subcomponent model parameters mentioned in Sec. II. A: the emergence of relationships between model parameters when constrained by experimental measurements. Goals of future

theoretical work ought to include justifying and explaining this empirically determined correlation.

The use of f_{dif} as an empirically calibrated flux limiter, and the enhanced ion thermal conduction, with f_{icnd} varying in the range 4 to 15 depending on fuel density, are signatures of “missing physics” in the RIK models. For example, the variation in f_{icnd} may be a result of neglecting ion enthalpy transport and frictional heating when f_{iht} is set to 0; ion conduction would then be forced to play the role of the neglected processes. In this case, new optimization studies using $f_{iht} \neq 0$ may reduce the variation in f_{icnd} . It is also likely that the two ion species in the fuel, D and ^3He , do not remain in temperature equilibrium during the passage of shock waves inward and outward through the fuel, particularly for the lower density capsules; the D ions are significantly less heated by the shocks than are the ^3He ions^{2,7,14}. The hydrodynamic code used for our simulations is a single-fluid code, forcing all species in a spatial mesh zone to have a single temperature. So it may be that the large values of f_{icnd} are the model’s way of giving the deuterium ions their relatively low observed temperature. The separation of species observed in our simulations, i.e., the preferential flow of D out of the fuel at a higher rate than ^3He (discussed in the next section), is another way that the model can force D to have a smaller mass-averaged temperature than ^3He .

C. Capsule structure in calibrated RIK simulations

Simulations using the RIK models, calibrated to match experimental measurements, typically have significantly different time-dependent capsule structure than do comparable clean simulations. This difference is manifestly the reason for the improved ability of RIK models to explain the experimental observations; the implication is that RIK simulations give a more accurate picture of the actual capsule structure during the experiment than do clean simulations. Figure 4 illustrates the difference. In Figure 4a is shown the structure of a RIK

simulation at about the time of peak shell implosion velocity, for a strongly kinetic capsule with a very low-density fill. The origin is on the left-hand boundary of the plot, and a shock wave in the D^3He fuel is propagating towards the left. The flow of D and 3He ions out of the shocked fuel region into the SiO_2 shell has led to intermixing of all four species over a wide region. Because D ions have longer mean free paths (larger collision time τ_s) than 3He ions, D flows into the shell more rapidly than 3He , leaving the shocked fuel depleted in D relative to 3He ; referring to Eq. 1 for τ_s , the mean free path of species s is $\lambda_s = \tau_s v_s \sim (T_i^{3/2} A_s^{1/2} / Z_s^2) (T_i / A_s)^{1/2} \sim T_i^2 / Z_s^2$, so λ_D is about four times larger than $\lambda_{^3He}$, in either a 50/50 D^3He mixture or a $\sim 100\%$ SiO_2 mixture. The ion temperature in the fuel is elevated far in front of the shockwave, owing to long-range ion thermal transport, extending all the way to the origin, and also far outward into the shell, about as far as the D ions have traveled.

In contrast, Figure 4b shows the structure of a clean simulation at the same time. There is no kinetic/diffusive intermixing of fuel ions and shell ions; the boundary between shell and fuel is effectively “sealed”, a quite unrealistic condition. As a result the fuel composition remains 50/50 D^3He everywhere. The postshock ion temperature is about a factor of two higher than in the RIK simulation, and the region of high T_i is confined only to the shocked fuel. Comparison with Figure 4a shows that the postshock 3He density is lower in the clean simulation than in the RIK simulation, where D has been depleted and 3He must support the majority of the momentum flux in the shock wave. Gradients of pressure, ion number density, and ion temperature are significantly larger in the clean simulation than in the RIK simulation, showing that, for example, estimates of the strength of ion thermodiffusion based on clean simulations may be inaccurate, at least at this time in the implosion. The clean simulation gives extremely poor estimates of observable quantities; for example, the D^3He yield is about $100\times$ higher than observed.³⁸

D. Consensus RIK models from multi-capsule calibration

Since the best-fit values of the two main RIK model parameters vary with capsule properties in Table II and Figure 3, it might be tempting to invent an additional model or rule that prescribes how to specify f_{icnd} and f_{idif} based on capsule parameters and evolution, when making predictions for a capsule experiment. For example, we could choose model parameters based on the initial fuel density, using the exponential fits shown as solid lines in Figure 3. Or parameters could be specified dynamically during the course of a simulation, according to an estimate of whether the imploding capsule is in the hydrodynamic or kinetic regime, based on the fuel-averaged Knudsen number. Rather than introduce such elaborations, however, we instead ask whether we can calibrate an optimum “consensus” set of RIK model parameters based on a fit to data from several capsule shots simultaneously. If we find that a single RIK model does an adequate job of explaining capsule behavior across a broad range of initial fuel density, then we can be more confident in using it for general predictions.

To fit several capsules simultaneously, we generalize Eq. 9 by summing over M distinct capsules:

$$S_{M,N}(\vec{f}) \equiv \sum_{k=1}^M \sum_{j=1}^N \frac{[Q_{kj,obs} - Q_{kj,sim}(\vec{f})]^2}{\sigma_{kj}^2}, \quad (10)$$

where index k identifies the different capsules, and we allow for the possibility that the uncertainty σ_{kj} in the j th observable varies from one capsule to another. Again, the optimization problem is to find the minimum of $S_{M,N}$ as the vector of RIK model parameters \vec{f} is varied. So long as the separate optimization searches for the individual capsules have all been conducted on the same grid in RIK model parameter space, it is easy to compute $S_{M,N}(f_{idif}, f_{icnd})$, for example, by summing the already available values of $S_N(f_{idif}, f_{icnd})$ for each capsule. This makes simultaneous optimization a simple process.

Fitting all eight shots in Table I simultaneously gives best-fit values $f_{dif}=0.1$ and $f_{icnd} = 4$. We refer to these input parameter values, together with the other fixed input parameters, as the “8-shot model.” The quality of the fit is measured by

$$\chi^2 \equiv \frac{\min_{\vec{f}} S_{M,N}(\vec{f})}{NM - n_{param} - 1},$$

where $N = 5$ is the number of observables per capsule, $M = 8$ is the number of capsules, and $n_{param} = 6$ is the number of non-zero model parameters. For the 8-shot model, $\chi^2 \cong 8.1$.

Simulation results using the 8-shot model were presented in Fig. 4 of the article by Rosenberg *et al.*¹³, where it is evident that the model explains the decrease of Y_{DDn} and Y_{D^3He} with decreasing initial fuel density rather well. Another attempt at a broad-range multiple-capsule fit is the “4-shot model”, using four of the shots having intermediate fuel density in the range 1.1 to 2.4 mg/cm³: shots 69057, 69058, 69061, and 69063. The resulting best-fit parameters are $f_{dif}=0.3$ and $f_{icnd} = 2$ with $\chi^2 \cong 6.3$.

Better fits are obtained when restricting the optimization to a more homogeneous set of capsule shots. Fitting only the three high-fuel-density shots 69055, 69057, and 69058 leads to $f_{dif} = 1(+0.7,-0.4)$ and $f_{icnd} = 1(+2.6,-0.5)$, with $\chi^2 \cong 2.8$. We call this the “high-fuel-density” model. The uncertainty range in f_{dif} is based on treating the three shots as repeated measurements of a single value of f_{dif} , whereas the uncertainty range in f_{icnd} is based on the widest variations obtained when fitting individual shots, allowing for a correlation of f_{icnd} with fuel density resulting from “missing physics”. Fitting only the five low-fuel-density shots 69061, 69063, 69064, 69066, and 69067, using the same prescription for uncertainty ranges, leads to $f_{dif} = 0.1(+0.06,-0.04)$ and $f_{icnd} = 8(+12,-6.5)$ with $\chi^2 \cong 4.2$. This is the “low-fuel-density” model.

Table III compares the parameter values for the four calibrated RIK models and a fifth model, the clean model, having $f_{Knu} = 0$, $f_{dif} = 0$, and $f_{icnd} = 1$. Figure 5 and Figure 6 show results of

simulations using all five models, in comparison to observations. All simulations assume a glass (SiO_2) capsule having 858- μm outer diameter, 2.3- μm ablator thickness, fuel composition $\text{D}:\text{}^3\text{He} = 0.4889:0.5111$ by atom, driven by a 14.9-kJ 0.6-ns square pulse. DD neutron yield is shown in Figure 5a, D^3He proton yield in Figure 5b, ion temperature inferred from DD neutrons in Figure 6a, and absorbed energy fraction in Figure 6b. Curves showing results from models are described in the figure captions.

E. (In)validation of calibrated RIK models

In the calibration/(in)validation process, after a model has been calibrated on one set of observations, the next step is to test the calibrated model against an independent set of observations, preferably from a different experimental scenario investigating a different physical regime. The degree of agreement between the new observations and calculations based on the model is a measure of the extent to which the model can be regarded as “not yet invalidated” for the new physical regime, and hence useful for making predictions. If a model is found to be useful (“not invalid”) in a variety of distinct physical regimes, we may begin to trust it to provide insight into the roles and importance of various physical mechanisms, and into the spatio-temporal structure of the implosions.

1. Deuterated-shell capsule implosions

To test the four calibrated RIK models identified in Sec. III.D., we used the observations of Rinderknecht *et al.*^{11,12}, who carried out implosions of thin-shell deuterated-plastic capsules. The capsules had $\sim 5\text{-}\mu\text{m}$ -thick shells with composition $\text{C}_1\text{D}_{1.4}$ (i.e. 41.7% C and 58.3% D atom fractions), and were filled with gas whose initial composition was varied from pure D_2 , to 50/50 D^3He by atom, to pure ^3He . The initial gas fill pressure was varied with composition in the range 3-4 atm, in order to keep the initial fuel density invariant at about 0.5 mg/cm^3 as the

composition was changed, thereby insuring that the implosions were “hydrodynamically equivalent” regardless of composition³⁹. The capsules were driven by a 1-ns square pulse delivering about 29 kJ of laser energy. Detailed parameters describing the three deuterated-shell capsules used for (in)validation, and their observed performance, are given in Table IV. Several measured quantities are shown for each capsule. When the gas contains no ^3He , the yield of secondary DT neutrons Y_{2DT} , which are difficult to detect if there is significant D^3He yield, is used as an observable. Uncertainties in the measured quantities were taken to be $\sigma_{YDD} = 10\%$, $\sigma_{YD^3\text{He}} = 10\%$, $\sigma_{Y2DT} = 43\%$, and $\sigma_{TiDD} = 0.5 \text{ keV}$.

These experiments are superficially similar to those of Rosenberg *et al.*¹³, on which the RIK models’ calibration was based, in the sense that both data sets came from 60-beam OMEGA direct-drive implosions, and both include measurements of DD and D^3He reactions in thin-shell capsules. But the deuterated-shell implosions differ significantly from the calibration experiments, particularly when the gas fill is pure ^3He , because in that case D^3He reactions occur only if there is intermixing of gas and shell material, only in the presence of a considerable population of ^{12}C ions, and typically at a large radius, distant from the hot central core of the capsule. The DD reactions likewise occur only in the shell or mixed region when the gas fill is pure ^3He . Even when the initial gas contains D_2 , the intermixed shell contributes a large fraction of the total D^3He yield. Therefore the deuterated-shell capsules, by comparison to the calibration experiments, impose an independent constraint on the flow of fuel ions into the shell; the calibration experiment’s yields depend on the loss of fuel ions by the fuel region, while the deuterated-shell experiment’s yields depend on the gain of fuel ions by the shell region.

To judge the validity of a model, we compute the difference between observed and calculated values of the three observable quantities for each capsule, as in Eq. 10, and then sum over all three deuterated-shell capsule experiments, to obtain $S_{3,3}$. For this purpose, simulations used the unique as-built dimensions and characteristics of each capsule as input. (In)validation

does not involve searching input parameter space; we compare only the five points in input space corresponding to the four calibrated RIK models and the clean model. Table V makes it clear that the high-fuel-density model has the smallest value of $S_{3,3}$ and is therefore “less invalid” than the other models, although the 4-shot model is not too much worse.

This judgment is borne out in Figure 7, which shows that the high-fuel-density model gives fairly good agreement with more of the data than do the other models, although the 4-shot model gives quite good agreement with observed D^3He yield in particular. All curves in the figure were calculated assuming a $C_1D_{1.4}$ shell having 866.0- μm outer diameter, 5.0- μm thickness, gas fill consisting of 3.02 atm pure D_2 , and laser energy 29.529 kJ in a 1-ns square pulse (the parameters for shot #65273). The clean model is clearly much less preferable overall than the other four, even though it gives a better fit for the equimolar capsule #65275 than one of the RIK models; this example serves as a warning, if one is needed, against drawing conclusions based on a single capsule experiment. Ultimately, whether any model is (in)valid for a particular application depends on the requirements of the application. If it is necessary to predict both the DD and D^3He yields in experiments such as these deuterated-shell shots with an accuracy of $\pm 10\%$, then none of the four RIK models is valid. But if an accuracy of a factor of two is acceptable, then both the high-fuel-density model and the 4-shot model are valid. Simulations using the 4-shot model were shown in Fig. 5 of the article by Rinderknecht *et al.*¹², together with simulations showing the effects of turning on various component models separately and in combination. For those simulations, a shell composition of C_1D_1 was used.

Although we shall not pursue it here, the next step in the calibration/(in)validation process would be to perform a re-calibration using the validation data simultaneously with the calibration data. We could thereby infer parameters for an improved model that would, we expect, give a better explanation of the entire set of data than either the high-fuel-density model or the 4-shot model alone. It seems plausible that such an improved model would have

parameter values intermediate between those of the high-fuel-density and the 4-shot models. We leave this step for future work.

2. Glass-shell composition-scan capsule implosions

As another (in)validation test of the four models identified above, we used an independent set of data obtained by Rinderknecht *et al.*¹⁴ on implosions of thin glass-shell capsules, in which again the composition of the D³He fuel was varied while maintaining hydrodynamic equivalency. These implosions differed from the (in)validation set discussed in the preceding section in that the shells had composition SiO₂, no deuterium was present in the shell, the pulse length was 0.6 ns, and capsules had either high fuel density (hydrodynamically equivalent to ~20 atm pure D₂) or low fuel density (hydrodynamically equivalent to ~2.4 atm pure D₂). The implosions differed from the calibration set in that the fuel composition varied from ³He-rich to equimolar D³He to ³He-poor, and that T_{iD^3He} , the observed average ion temperature determined from D³He reactions, is available for comparison to simulations. (T_{iD^3He} was not used as a constraint on the models during calibration.) Detailed parameters describing this set of capsules, and their observed performance, are given in Table VI.

All four calibrated RIK models were used to calculate the dependence of various observables on fuel deuterium atom fraction, f_D , for these capsules, for high fuel density as well as low fuel density. In all simulations, the capsule was assumed to have 854- μ m outer diameter, 2.2- μ m ablator thickness, and to be driven by a 14.6-kJ 0.6-ns square pulse. Simulations for high fuel density used fill pressure hydrodynamically equivalent to 19.0 atm pure D₂. Simulations for low fuel density used fill pressure hydrodynamically equivalent to 2.4 atm pure D₂. Results are shown in

Figure 8 (high fuel density) and Figure 9 (low fuel density). We have not calculated quantitative (in)validation metrics for these comparisons, but it is qualitatively clear from

Figure 8 that, not surprisingly, the high-fuel-density model is preferable for the ~ 20 -atm fills, and from Figure 9 that the low-fuel-density model is preferable for the ~ 2.4 -atm fills, though the 8-shot model is comparable. The general agreement between these models and the data is also not surprising, given that the equimolar calibration shots on which the high-fuel-density and low-fuel-density models are based are very similar to the shots in

Figure 8 and Figure 9 at $f_D = 0.5$. The (in)validation data base thus mainly tests the models' ability to predict the effect of excursions in the fuel composition around $f_D = 0.5$, extending as low as $f_D = 0.2$ and as high as $f_D = 1$; it also tests the models' ability to predict an observable not used as a calibration constraint, i.e., T_{iD^3He} .

The most notable discrepancy between observations and calculations in

Figure 8 and Figure 9 is seen for T_{iD^3He} . In

Figure 8d, all models give calculated values of T_{iD^3He} that are significantly smaller than observed. In Figure 9d, no matter which of the four RIK models is used, calculations show T_{iD^3He} decreasing as f_D increases, while observations show instead that T_{iD^3He} is roughly constant or even increasing as f_D increases. It is possible that some of the discrepancy can be explained by the different definitions of this quantity according to whether it is empirically or calculationally determined. In experiments, T_{iD^3He} is determined from the width of the thermal-Doppler-broadened spectrum of protons created in D^3He reactions, with birth energy of 14.7 MeV, which are slightly downshifted in energy because of their passage out of the capsule. In simulations, however, T_{iD^3He} is calculated as the time- and space-averaged ion temperature, enforced to be equal for all species, but weighted by the local rate of D^3He reactions. (In principle it is possible to compute the emergent spectrum of D^3He protons, accounting for the temporal and spatial variation in their production rate and their transport out of the capsule, but this is rarely done in practice.)

Rinderknecht *et al.*¹⁴ interpret the T_{iD^3He} discrepancy as evidence for thermal decoupling of D and ^3He ions in these strongly shock-driven “exploding pusher” capsules. They show that the timescale for thermal equilibration of D and ^3He , and the individual self-thermalization timescale of each species, are long compared to the burn duration for the low-density capsules. The RIK models, however, enforce temperature equality among all ion species in a computational mesh cell, and therefore cannot directly represent ion thermal nonequilibrium.⁴⁰ Rinderknecht *et al.*¹⁴ develop a simple model for the average ion temperatures that accounts for temperature nonequilibrium and show that it explains the observations. This seems like a valid conclusion, and is reinforced by the recent results of Inglebert *et al.*³, who find evidence for temperature nonequilibrium in cryogenic non-igniting implosions at NIF. A re-calibration of RIK models for the D ^3He implosions using T_{iD^3He} as a constraint, if they still fail to explain the data, would lend yet more confidence to the conclusion.

IV. Summary and Conclusions

We have described the class of *reduced ion-kinetic* (RIK) models, consisting of the Schunk-Zimmerman moment-based gradient-diffusion transport model, the Molvig-Albright fusion-reactivity-reduction model, and the Dimonte hydrodynamic turbulent mixing model, implemented and running simultaneously in a radiation-hydrodynamic code. RIK models are characterized by the values of a number of parameters, introduced in Secs. I and II, which can be calibrated using experimental observations. Calibrated models are useful for predicting or interpreting results from experiments under conditions that vary from the calibration conditions. We showed that several models calibrated using data from thin glass-shell capsule implosions with varying initial fuel density (Secs. III.B and III.D) led to useful explanations of data from independent experiments: thin deuterated-plastic shell capsules with varying fuel composition (Sec. III.E.1) and thin glass-shell capsules with varying fuel composition (Sec.

III.E.2). For example, the “4-shot” model calibrated on glass-shell capsules from Ref. 13 can explain (and could have predicted) observables from the deuterated plastic-shell capsules of Refs. 11 and 12, such as Y_{DDn} (within $2\times$), Y_{D3He} (within 10%), and T_{iDD} (within 15%). But we found that no single RIK model gives as good an explanation of capsule performance across a range of initial fuel densities as do separate RIK models individually calibrated for each fuel density.

Calibrated RIK models are also useful for the insight they afford into the time-dependent structure of capsules throughout their implosion. They show that, in the kinetic regime, shocked fuel ions flow outward into the imploding shell at a high rate, depleting the fuel volume and leading to much lower fusion yields than implied by clean simulations. The outflow is species-dependent, with less highly charged ions (such as D) flowing at a significantly higher rate than more highly charged ions (such as ^3He); the resulting ion species segregation leaves the fuel enriched in the more highly charged species. Transport of ion thermal energy is also enhanced in the kinetic regime, causing the fuel region to have a more uniform, lower ion temperature, extending over a larger volume, than implied by clean simulations. Ion thermal energy is carried outward into the shell as well, by the escaping fuel ions.

The RIK model class as defined here leaves something to be desired in its predictive capability as initial fuel density is varied across the transition from the hydrodynamic regime to the kinetic regime. After all, we regard this model as *schematic*, in the sense of providing an outline or “rough draft” of a complete first-principles-based model. Its four main approximations are (1) the use of an average collisional drag over all species, with an associated collision time scale τ_s , (2) the neglect of the ion thermodiffusion force, (3) the lack of flux limiters in the ion mass flux model, and (4) the *a priori* independence of the component models’ parameters. These approximations clearly define directions for further research leading to improved models. We expect that the successful application of RIK models as described in this

article, approximate as these models are, will encourage continued development of first-principles-based, comprehensive, self-consistent, yet useable models of kinetic multispecies ion behavior in ICF plasmas.

V. Acknowledgements

We are grateful to a number of individuals for advice and discussions concerning this work: Evan Dodd for advice about scattered-light measurements and their importance; Erik Vold for explanations of the scaling of the ion transport equations; and Hans Herrmann, Yong-Ho Kim, Colin Horsfield (AWE), and Mike Rubery (AWE) for discussions of simulations and data from other experiments. This project was supported by the U.S. Department of Energy under contract DE-AC52-06NA25396.

Table I. Capsule parameters and data for calibration (Rosenberg *et al.*¹³)
Glass-shell pressure-scan implosions, 0.6-ns square pulse

OMEGA shot #	Diam (μm)	Thick (μm)	D ₂ press (atm)	³ He press (atm)	total press (atm)	fuel density (mg/cm ³)	E_L (kJ)	Y_{DDn} (10 ¹⁰)	Y_{D^3He} (10 ¹⁰)	T_{iDD} (keV)	t_b (ps)	f_{abs} (%)
69055	854	2.2	8.37	14.13	22.50	3.12	14.6	2.81	3.40	12.2	730	59
69057	869	2.2	5.70	11.24	16.94	2.35	14.5	2.35	3.60	12.8	752	57
69058	835	2.4	5.70	10.32	16.02	2.22	14.6	2.60	4.00	12.4	760	55
69061	840	2.2	2.56	5.61	8.18	1.13	14.3	1.32	3.30	12.9	738	60
69063	858	2.3	2.56	5.36	7.92	1.10	14.9	1.70	3.90	14.0	743	56
69064	861	2.3	1.61	3.23	4.84	0.67	15.0	1.05	2.90	15.8	711	56
69066	868	2.3	0.96	1.92	2.88	0.40	14.8	0.548	2.30	19.5	738	55
69067	859	2.3	0.34	0.68	1.02	0.14	14.7	0.0724	0.480	19.9	731	56

Uncertainties in observables are $\sigma_{YDD} = 10\%$, $\sigma_{YD^3He} = 10\%$, $\sigma_{T_{iDD}} = 2 \text{ keV}$, $\sigma_{t_b} = 50 \text{ ps}$, and $\sigma_{f_{abs}} = 4\%$.

Table II. Best-fit RIK parameters with uncertainty ranges for MIT glass-shell pressure-scan capsules

$$[f_{ls} = 0.63, f_e = 0.06, f_{Knu} = 0.1, f_{iflxm} = 1, f_{ivis} = f_{iht} = f_{Te} = l = 0]$$

OMEGA shot #	diameter (μm)	total press (atm)	fuel density (mg/cm^3)	f_{dif}	f_{icnd}
69055	854	22.50	3.12	1.0 (+1.2, -0.3)	1.0 (+0.6, -0.4)
69057	869	16.94	2.35	0.8 (+0.6, -0.4)	1.0 (+1.6, -0.5)
69058	835	16.02	2.22	1.0 (+0.5, -0.4)	2.0 (+1.6, -1.2)
69061	840	8.18	1.13	0.2 (+0.09, -0.06) ^a	4.0 (+3.4, -2.5) ^a
69063	858	7.92	1.10	0.2 (+0.05, -0.04)	4.0 (+2.2, -2.1)
69064	861	4.84	0.67	0.1 (+0.1, -0.03) ^a	8 (+12, -5) ^a
69066	868	2.88	0.40	0.1 \pm 0.06	6 (+9, -4)
69067	859	1.02	0.14	0.1 \pm 0.04	15 (+5, -7)

Uncertainty range of best-fit f_{dif} and f_{icnd} is based on size of $D_5 = 1.5\sqrt{5}$ contour, i.e., a 1.5σ fit.

^a For shots #69061 and #69064, uncertainty range is based on a 2σ fit.

Table III. Non-zero parameters for RIK models calibrated on multiple MIT glass-shell pressure-scan capsules¹³

(All models have $f_{ivis} = f_{iht} = f_{Te} = l = 0$)

Model name	f_{ls}	f_e	f_{iflsm}	f_{Knu}	f_{idif}	f_{icnd}
High-fuel density	0.63	0.06	1	0.1	1	1
4-shot	0.63	0.06	1	0.1	0.3	2
Low-fuel-density	0.63	0.06	1	0.1	0.1	8
8-shot	0.63	0.06	1	0.1	0.1	4
Clean	0.63	0.06	1	0	0	1

Table IV. Capsule parameters and data for model (in)validation
(Rinderknecht *et al.*^{11,12})

Deuterated-shell implosions, 1-ns square pulse

OMEGA shot #	Diam (μm)	thick (μm)	D ₂ press (atm)	³ He press (atm)	deuterium atom frac f_D	total press (atm)	fuel density (mg/cm ³)	E_L (kJ)	Y_{DDn} (10 ¹⁰)	Y_{D^3He} (10 ¹⁰)	Y_{2DT} (10 ⁶)	T_{iDD} (keV)
65273	866	5.0	3.02	0.0	1.0	3.02	0.50	29.529	7.39	-----	7.1	16.3
65275	856.2	5.1	1.25	2.44	0.51	3.69	0.54	29.275	3.73	3.76	-----	15.5
65278	877.2	5.1	0.0	4.05	0.0	4.05	0.51	29.455	1.52	2.97	-----	13.8

Uncertainties in the observables are $\sigma_{YDD} = 10\%$, $\sigma_{YD^3He} = 10\%$, $\sigma_{Y2DT} = 43\%$, and $\sigma_{T_{iDD}} = 0.5$ keV.

Table V. Model comparisons for (in)validation studyDeuterated-shell implosions^{11,12}Simulations used as-shot shell composition C₁D_{1.4}(For each capsule, table shows $D_3 \equiv \sqrt{S_3}$ for each model.)

OMEGA shot #	deuterium atom frac f_D	8-shot model	4-shot model	High-fuel- density model	Low-fuel- density model	Clean model
65273	1.0	12.28	6.33	5.59	13.62	17.84
65275	0.51	9.08	6.02	5.53	13.71	10.40
65278	0.0	10.79	5.68	3.69	16.20	99.16
$\sqrt{S_{3,3}}$		18.70	10.42	8.68	25.22	101.29

Table VI. Capsule parameters and data for 2nd (in)validation study (Rinderknecht *et al.*¹⁴)
(Sorted by fuel pressure and by composition)
Glass-shell composition-scan implosions, 0.6-ns square pulse

OMEGA shot #	Inner diam (μm)	Thick (μm)	D ₂ press (atm)	³ He press (atm)	total press (atm)	f_D	fuel density (mg/cm ³)	E_L (kJ)	Y_{DDn} (10 ¹⁰)	Y_{D^3He} (10 ¹⁰)	T_{iDD} (keV)	T_{iD^3He} (keV)	t_b (ps)	f_{abs} (%)
69257	868.5	2.3	0.37	2.96	3.33	0.20	0.42	14.36	0.062	1.02	20.75	23.84	700	0.58
69251	845.1	2.4	0.37	2.64	3.00	0.22	0.39	14.65	0.077	1.19	17.79	21.76	700	0.57
69254	844.4	2.3	0.96	1.85	2.81	0.51	0.39	14.60	0.493	2.00	16.46	23.82	691	0.54
69249	883.2	2.3	0.96	1.84	2.80	0.51	0.38	14.52	0.525	2.19	18.74	23.41	654	0.60
69256	853.0	2.2	1.83	0.81	2.64	0.82	0.40	14.69	1.99	2.16	18.28	25.17	665	0.55
69250	845.6	2.3	1.83	0.72	2.55	0.84	0.39	14.65	2.07	2.13	18.76	25.05	684	0.57
69263	836.3	2.3	2.38	0.00	2.38	1.00	0.39	14.45	3.73	-----	18.83	-----	717	0.55
69258	858.4	2.4	2.38	0.00	2.38	1.00	0.39	14.58	3.43	-----	18.64	-----	694	0.57
69259	836.2	2.2	2.38	0.00	2.38	1.00	0.39	14.62	2.50	-----	18.30	-----	663	0.54
69265	881.0	2.2	7.92	16.88	24.80	0.48	3.38	14.84	2.20	3.39	12.18	16.32	748	0.59
69264	869.2	2.2	7.92	15.22	23.15	0.51	3.17	14.71	2.35	3.71	11.56	15.89	725	0.58
69252	852.3	2.4	15.64	5.95	21.59	0.84	3.30	14.56	11.8	2.71	10.91	12.91	772	0.58
69261	878.6	2.4	20.13	0.00	20.13	1.00	3.30	14.56	21.8	-----	10.80	-----	779	0.60
69262	846.2	2.3	20.13	0.00	20.13	1.00	3.30	14.63	21.0	-----	10.80	-----	750	0.55

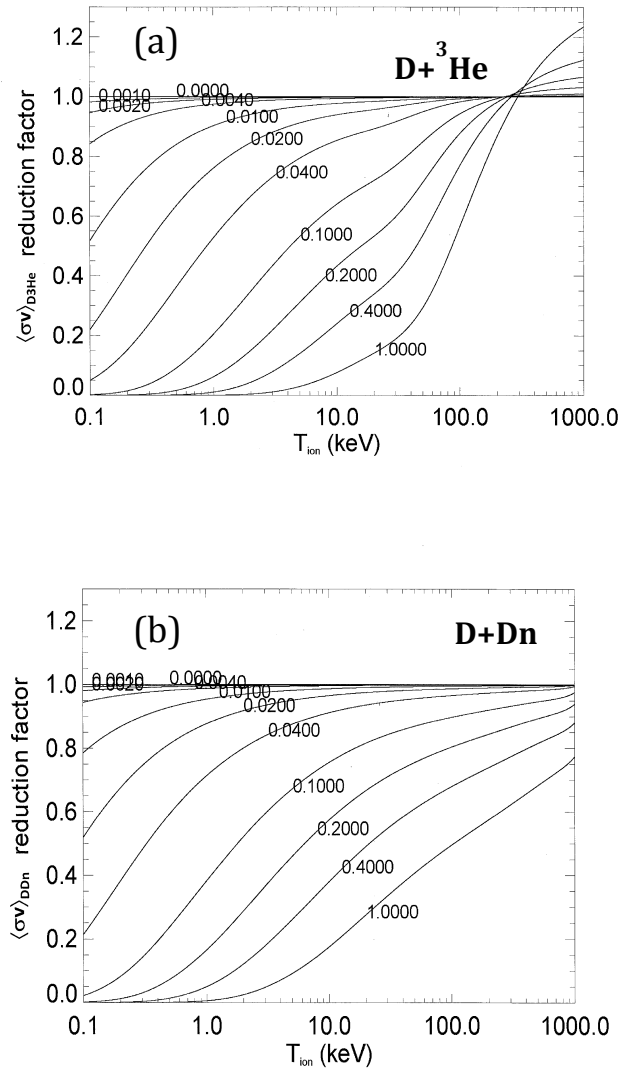


Figure 1. Fusion reactivity reduction ratio $\langle\sigma v\rangle(T_i, N_{Kp})/\langle\sigma v\rangle(T_i, 0)$ for D^3He (Fig. 1a) and $\text{D}+\text{Dn}$ (Fig. 1b) reactions. Curves are labeled with proton Knudsen number N_{Kp} .

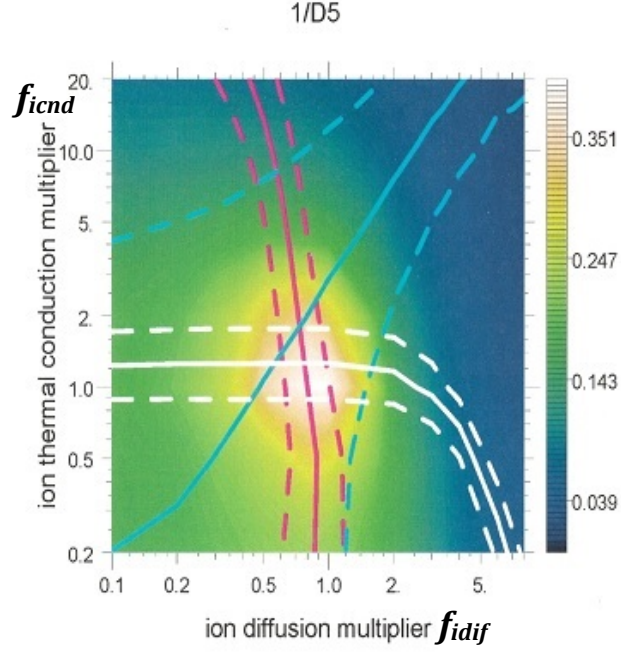


Figure 2. Contours of the reciprocal of $D_5 \equiv \sqrt{S_5}$ on a 2D projection of input space with axes f_{idif} and f_{icnd} , for an OMEGA capsule implosion experiment (shot #69057) in which five quantities were measured: Y_{DDn} , Y_{D^3He} , T_{iDD} , t_b , and f_{abs} . Solid lines show loci on which the difference between observation and simulation vanishes, for Y_{DDn} (red), Y_{D^3He} (white), and T_{iDD} (blue). Dashed lines show loci on which the difference between observation and simulation equals $\pm 1\sigma$. D_5 is minimized at $f_{idif} = 0.8$, $f_{icnd} = 1.0$.

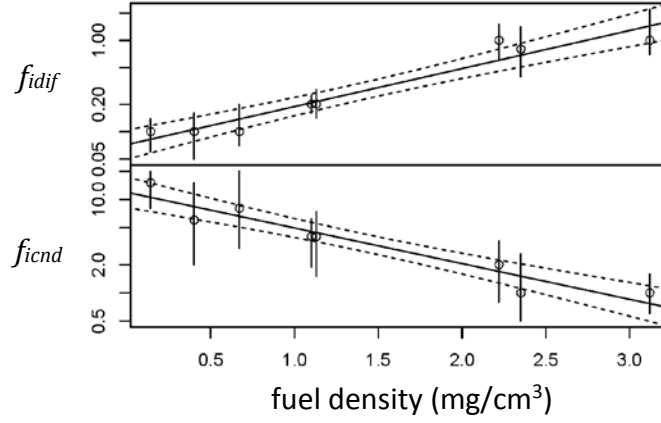


Figure 3. Dependence of best-fit RIK parameters f_{idif} and f_{icnd} on initial fuel density of thin glass-shell capsules¹³. Best-fit values of f_{idif} and f_{icnd} are clearly correlated. High-density capsules have f_{idif} and f_{icnd} near unity while low-density capsules have $f_{idif} \ll 1$ and $f_{icnd} \gg 1$. These results are also tabulated in Table II.

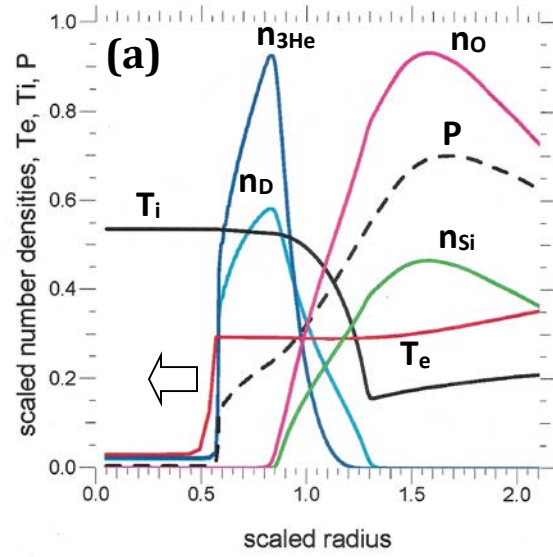


Figure 4a. Capsule structure at time of peak shell velocity from RIK simulation ($f_{Knu} = 0.1$, $f_{dif} = 0.1$, $f_{icnd} = 15$) giving a good fit to the observations for shot #69067 (~ 1 -atm gas fill). Radial coordinate is scaled by radius of fuel/shell interface in clean simulation (Figure 4b).

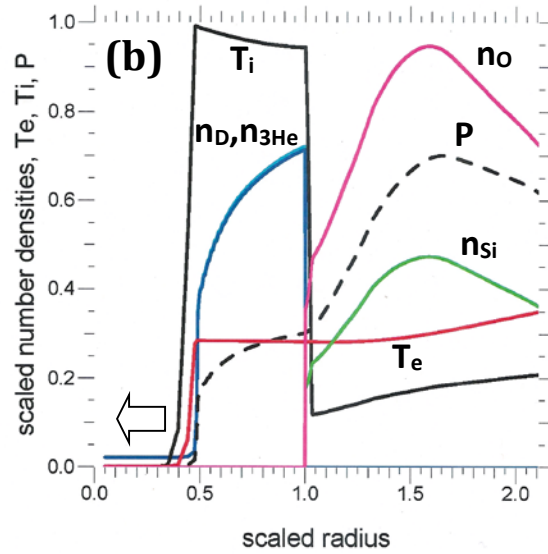


Figure 4b. Capsule structure at time of peak shell velocity from "clean" simulation using same parameter values as in Fig. 3a, except for $f_{Knu} = 0$, $f_{dif} = 0$, $f_{icnd} = 1$. Scale is same as in Figure 4a.

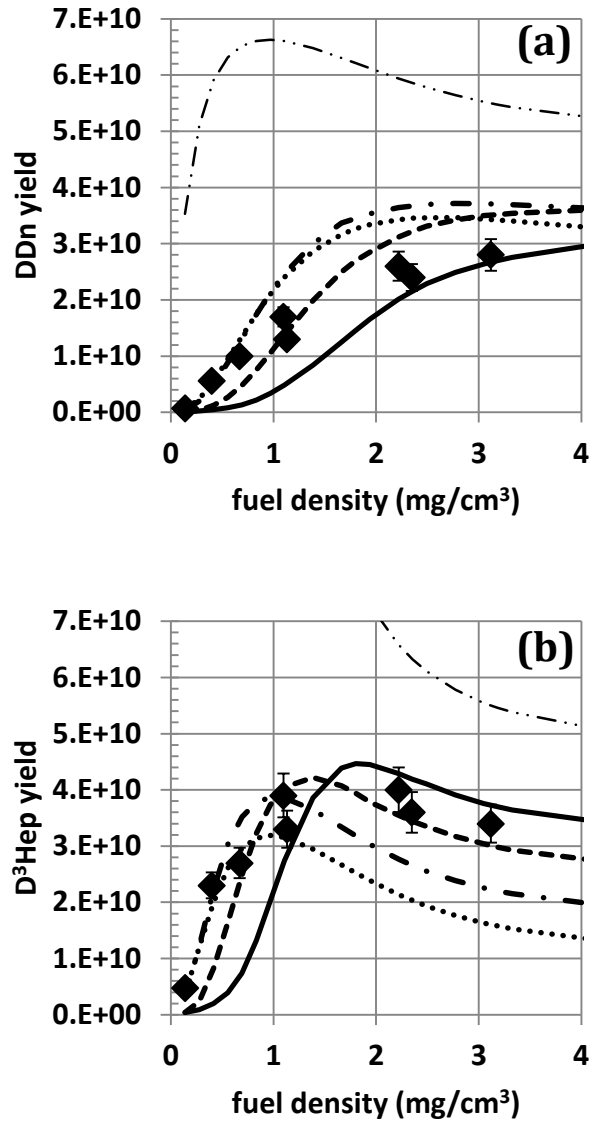


Figure 5. Comparison of observations of glass-shell pressure-scan capsules to simulated results using four calibrated RIK models. (a) DD neutron yield, (b) D³He proton yield. Solid symbols show Rosenberg *et al.*'s observations¹³; solid line is high-fuel-density model; dotted line is low-fuel-density model; dashed line is 4-shot model; dash-dot line is 8-shot model; light dash-double-dot line is clean model.

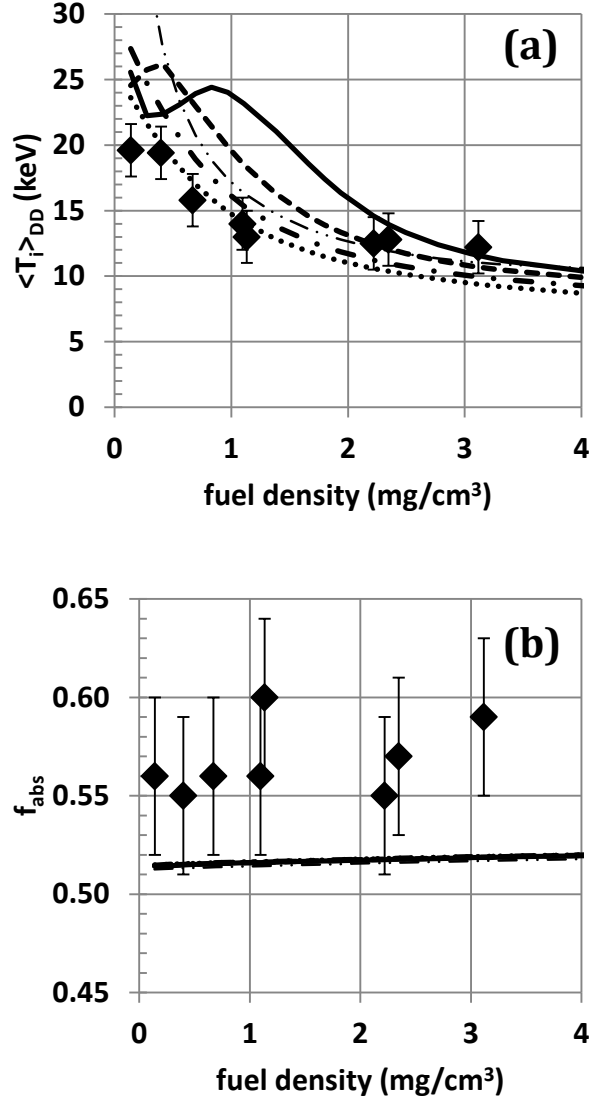
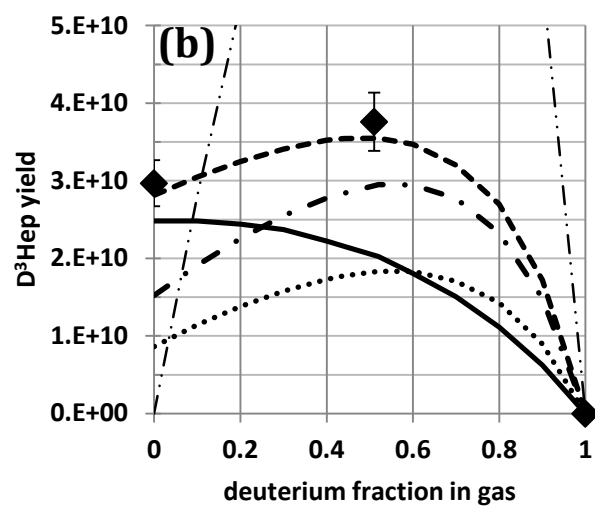
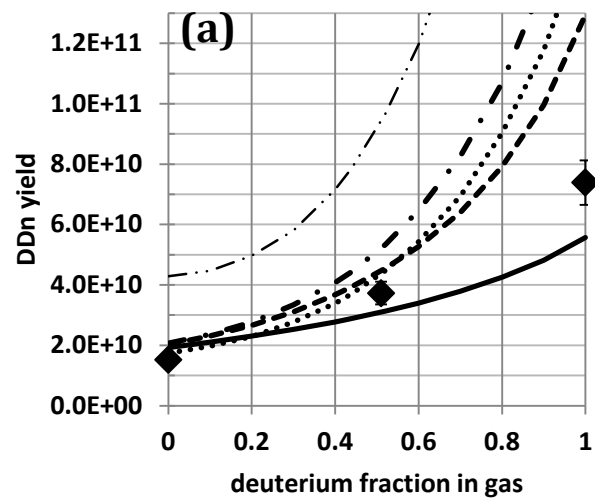


Figure 6. Comparison of observations of glass-shell pressure-scan capsules to simulated results using four calibrated RIK models. (a) ion temperature inferred from DD neutrons, (b) absorbed energy fraction. Solid symbols show Rosenberg *et al.*'s observations¹³; solid line is high-fuel-density model; dotted line is low-fuel-density model; dashed line is 4-shot model; dash-dot line is 8-shot model; light dash-double-dot line is clean model.



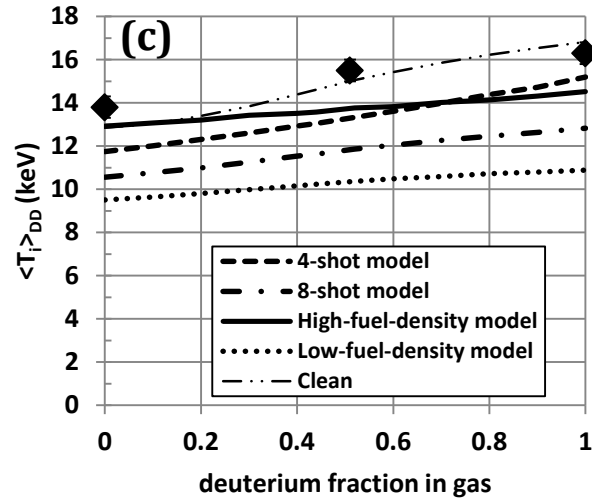
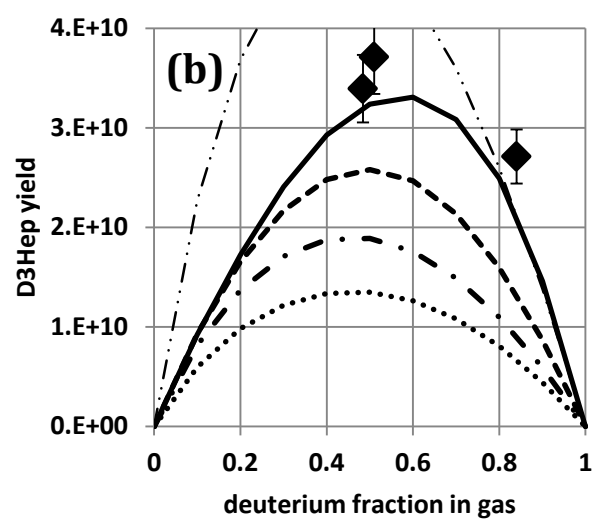
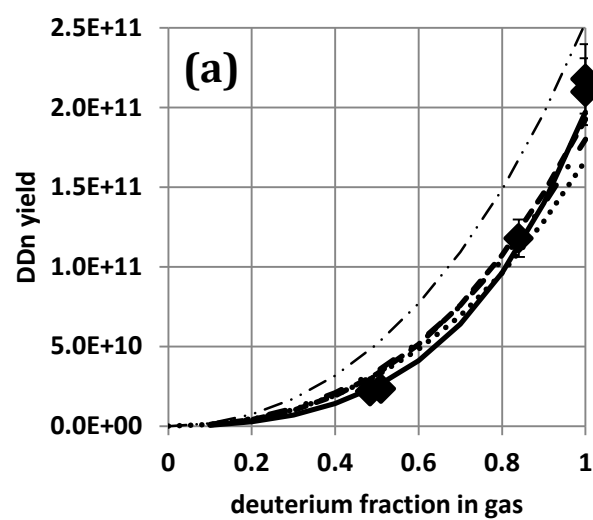


Figure 7. Comparisons of measurements of hydrodynamically equivalent 3-4 atm deuterated-shell capsule implosions to simulated results using four RIK models calibrated on glass-shell pressure-scan data¹³. (a) DD neutron yield, (b) D³He proton yield, (c) ion temperature inferred from DD neutrons. Solid symbols show Rinderknecht *et al.*'s observations^{11,12}; solid line is high-fuel-density model; dotted line is low-fuel-density model; dashed line is 4-shot model; dash-dot line is 8-shot model; light dash-double-dot line is clean model. Simulations used as-shot shell composition C₁D_{1.4}.



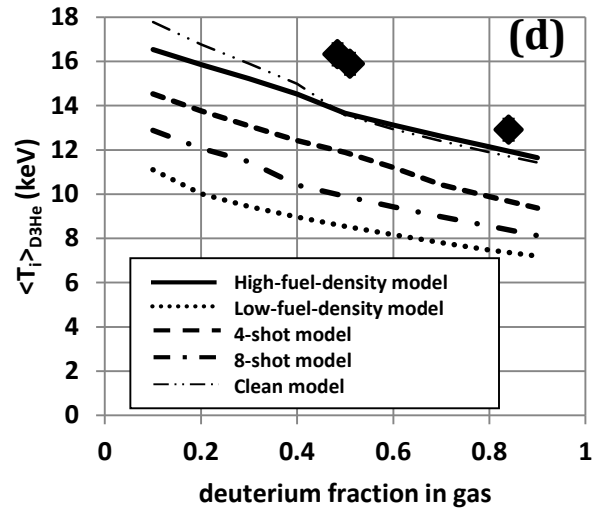
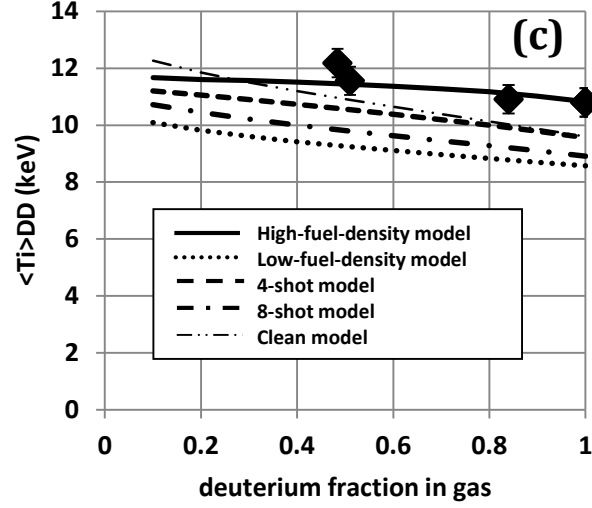
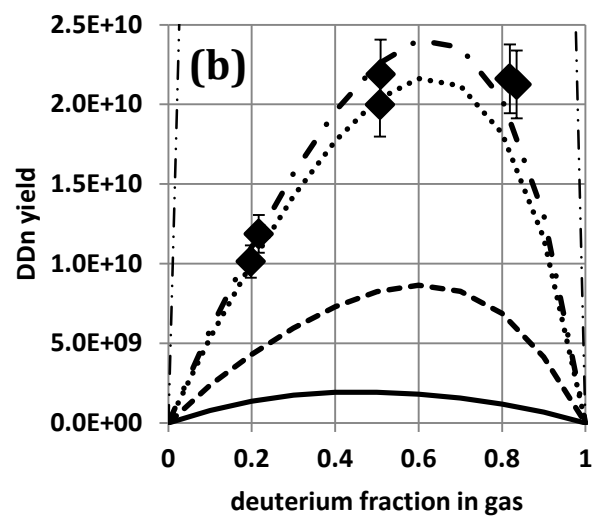
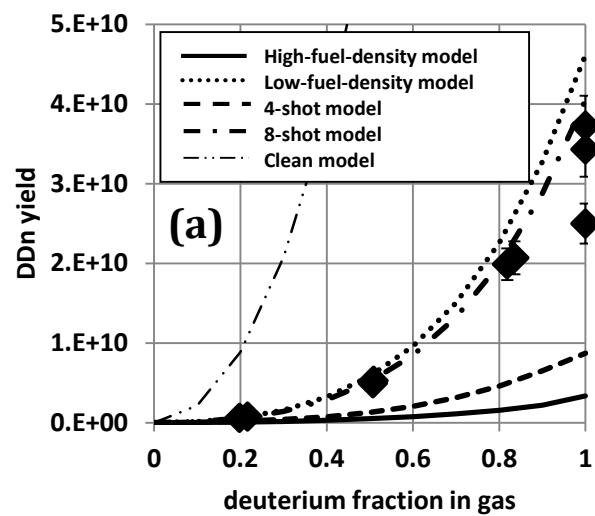


Figure 8. Comparisons of measurements of glass-shell composition-scan capsule implosions containing high-density ($\sim 3.3 \text{ mg/cm}^3$) fuel to simulated results using four RIK models calibrated on glass-shell pressure-scan data¹³. (a) DD neutron yield, (b) D^3He proton yield, average ion temperature inferred from (c) DD neutrons and (d) D^3He protons. Solid symbols show Rinderknecht *et al.*'s observations¹⁴; solid line is high-fuel-density model; dotted line is low-fuel-density model; dashed line is 4-shot model; dash-dot line is 8-shot model; light dash-double-dot line is clean model.



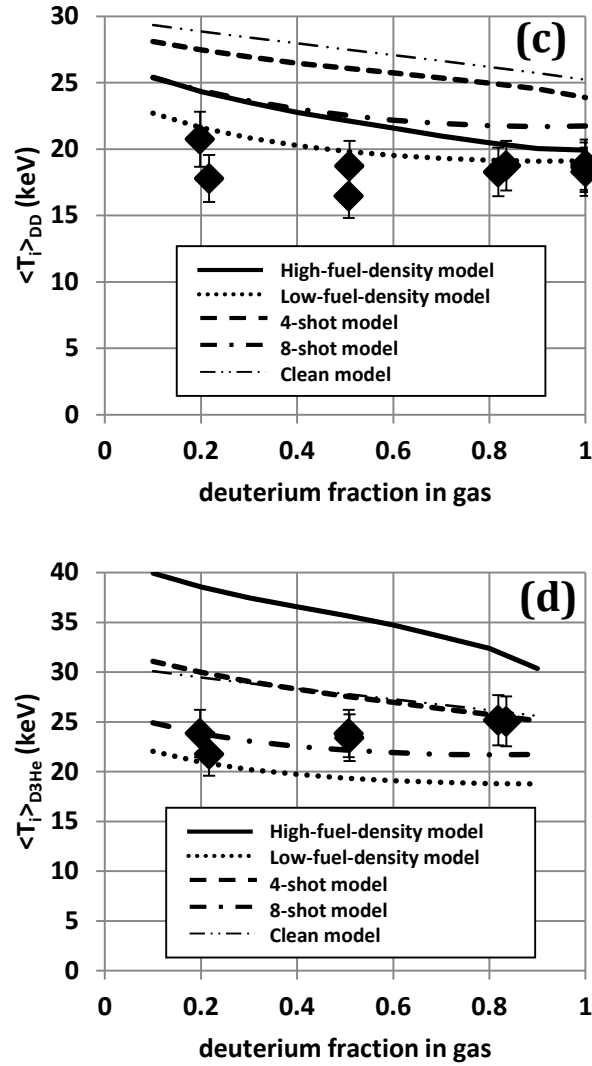


Figure 9. Comparisons of measurements of glass-shell composition-scan capsule implosions containing low-density ($\sim 0.4 \text{ mg/cm}^3$) fuel to simulated results using four RIK models calibrated on glass-shell pressure-scan data¹³. (a) DD neutron yield, (b) $D^3\text{He}$ proton yield, average ion temperature inferred from (c) DD neutrons and (d) $D^3\text{He}$ protons. Solid symbols show Rinderknecht *et al.*'s observations¹⁴; solid line is high-fuel-density model; dotted line is low-fuel-density model; dashed line is 4-shot model; dash-dot line is 8-shot model; light dash-double-dot line is clean model.

-
- ¹ A. G. Petschek and D. B. Henderson, *Nucl. Fusion* **19**, 1678 (1979).
- ² O. Larroche, *Eur. Phys. J. D* **27**, 131 (2003); O. Larroche, *Phys. Plasmas* **19**, 122706 (2012).
- ³ A. Inglebert, B. Canaud, O. Larroche, *EPL* **107**, 65003 (2014).
- ⁴ K. Molvig, N. M. Hoffman, B. J. Albright, E. M. Nelson, R. B. Webster, *Phys. Rev. Lett.* **109**, 095001 (2012).
- ⁵ B. J. Albright, K. Molvig, C.-K. Huang, A. N. Simakov, E. S. Dodd, N. M. Hoffman, G. Kagan, and P. F. Schmit, *Phys. Plasmas* **20**, 122705 (2013).
- ⁶ P. F. Schmit, K. Molvig, and C. W. Nakhleh, *Phys. Plasmas* **20**, 112705 (2013)
- ⁷ C. Bellei, P. A. Amendt, S. C. Wilks, M. G. Haines, D. T. Casey, C. K. Li, R. Petrasso, and D. R. Welch, *Phys. Plasmas* **20**, 012701 (2013); C. Bellei and P. A. Amendt, *Phys. Rev. E* **90**, 013101 (2014).
- ⁸ S. Davidovits and N. J. Fisch, *Phys. Plasmas* **21**, 092114 (2014).
- ⁹ B. I. Cohen, A. M. Dimits, G. B. Zimmerman, and S. C. Wilks, *Phys. Plasmas* **21**, 122701 (2014)
- ¹⁰ X.-Z. Tang, H. L. Berk, Z. Guo, and C. J. McDevitt, *Phys. Plasmas* **21**, 032707 (2014); X.-Z. Tang, C. J. McDevitt, Z. Guo, and H. L. Berk, *Phys. Plasmas* **21**, 032706 (2014); X.-Z. Tang, C. McDevitt, Z. Guo, and H. L. Berk, *Eur. Phys. Lett.* **105**, 32001 (2014).
- ¹¹ H. G. Rinderknecht, H. Sio, C. K. Li, A. B. Zylstra, M. J. Rosenberg, P. Amendt, J. Delettrez, C. Bellei, J. A. Frenje, M. Gatu Johnson, F. H. Séguin, R. D. Petrasso, R. Betti, V. Yu. Glebov, D. D. Meyerhofer, T. C. Sangster, C. Stoeckl, O. Landen, V. A. Smalyuk, S. Wilks, A. Greenwood, and A. Nikroo, *Phys. Rev. Lett.* **112**, 135001 (2014).
- ¹² H. G. Rinderknecht, H. Sio, C. K. Li, N. Hoffman, A. B. Zylstra, M. J. Rosenberg, J. A. Frenje, M. Gatu Johnson, F. H. Séguin, R. D. Petrasso, R. Betti, V. Yu. Glebov, D. D. Meyerhofer, T. C. Sangster, W. Seka, C. Stoeckl, G. Kagan, K. Molvig, C. Bellei, P. Amendt, O. Landen, J. R. Rygg, V. A. Smalyuk, S. Wilks, A. Greenwood, and A. Nikroo, *Phys. Plasmas* **21**, 056311 (2014).

¹³ M. J. Rosenberg, H. G. Rinderknecht, N. M. Hoffman, P. A. Amendt, S. Atzeni, A. B. Zylstra, C. K. Li, F. H. Séguin, H. Sio, M. Gatu Johnson, J. A. Frenje, R. D. Petrasso, V. Yu. Glebov, C. Stoeckl, W. Seka, F. J. Marshall, J. A. Delettrez, T. C. Sangster, R. Betti, V. N. Goncharov, D. D. Meyerhofer, S. Skupsky, C. Bellei, J. Pino, S. C. Wilks, G. Kagan, K. Molvig, and A. Nikroo, *Phys. Rev. Lett.* **112**, 185001 (2014).

¹⁴ H. G. Rinderknecht, M.J. Rosenberg, C.K. Li, N. M. Hoffman, G. Kagan, A.B. Zylstra, H. Sio, J.A. Frenje, M. Gatu Johnson, F.H. Séguin, R.D. Petrasso, P. Amendt, C. Bellei, S. Wilks, J. Delettrez, V. Yu. Glebov, C. Stoeckl, T.C. Sangster, D.D. Meyerhofer, and A. Nikroo, *Phys. Rev. Lett.* **114**, 025001 (2015).

¹⁵ M. J. Rosenberg, A. B. Zylstra, F. H. Séguin, H. G. Rinderknecht, J. A. Frenje, M. Gatu Johnson, H. Sio, C. J. Waugh, N. Sinenian, C. K. Li, R. D. Petrasso, P. W. McKenty, M. Hohenberger, P. B. Radha, J. A. Delettrez, V. Yu. Glebov, R. Betti, V. N. Goncharov, J. P. Knauer, T. C. Sangster, S. LePape, A. J. Mackinnon, J. Pino, J. M. McNaney, J. R. Rygg, P. A. Amendt, C. Bellei, L. R. Benedetti, L. Berzak Hopkins, R. M. Bionta, D. T. Casey, L. Divol, M. J. Edwards, S. Glenn, S. H. Glenzer, D. G. Hicks, J. R. Kimbrough, O. L. Landen, J. D. Lindl, T. Ma, A. MacPhee, N. B. Meezan, J. D. Moody, M. J. Moran, H.-S. Park, B. A. Remington, H. Robey, M. D. Rosen, S. C. Wilks, R. A. Zacharias, H. W. Herrmann, N. M. Hoffman, G. A. Kyrala, R. J. Leeper, R. E. Olson, J. D. Kilkenny, and A. Nikroo, *Phys. Plasmas* **21**, 122712 (2014).

¹⁶ The reactivity model was used along with a model of hydrodynamic turbulent mixing to explain the values of three observed quantities (DT neutron yield Y_{DT} , average ion temperature T_{iDT} over the period when DT fusion reactions occurred, and “bang time” t_b , the time of peak fusion reaction rate relative to the beginning of the laser pulse) for a set of eleven plastic-shell DT-filled capsules spanning $2\frac{1}{2}$ decades in Y_{DT} , a factor of four in T_{iDT} , and a factor of two in t_b .

¹⁷ V. N. Goncharov, O. V. Gotchev, E. Vianello, T. R. Boehly, J. P. Knauer, P. W. McKenty, P. B.

Radha, S. P. Regan, T. C. Sangster, S. Skupsky, V. A. Smalyuk, R. Betti, R. L. McCrory, D. D.

Meyerhofer, C. Cherfils-Clerouin, *Phys. Plasmas* **13**, 012702 (2006).

¹⁸ I. V. Igumenshev, D. H. Edgell, V. N. Goncharov, J. A. Delettrez, A. V. Maximov, J. F. Myatt, W.

Seka, A Shvydky, S. Skupsky, C. Stoeckl, *Phys. Plasmas* **17**, 122708 (2010).

¹⁹ E. S. Dodd, J. F. Benage, G. A. Kyrala, D. C. Wilson, F. J. Wysocki, W. Seka, V. Yu. Glebov, C.

Stoeckl, J. A. Frenje, *Phys. Plasmas* **19**, 042703 (2012).

²⁰ A flux limiter is an approximation that prevents the flux of a quantity Φ , with volume density ϕ , from exceeding the “streaming limit” $v_{th}\phi$ when the spatial gradient of ϕ is large, i.e., when the mean free path λ of ions transporting Φ is large compared to the gradient scale length $s \equiv [\nabla \phi / \phi]^{-1}$. Here v_{th} is the mean velocity of the ions transporting Φ . Flux limiters have traditionally been implemented by computational physicists as heuristic “fix-ups”, lacking a rigorous basis, although Levermore and Pomraning [Ap. J **248**, 321 (1981)] have put flux limiters on a firmer foundation for the case of transport by single-speed particles whose distribution function has angular dependence that varies slowly in space and time.

²¹ R. W. Schunk, *Rev. Geophys. Space Physics* **15**, 429 (1977).

²² G. Zimmerman, unpublished notes (1978, 2000).

²³ The eight moments, for each ion species, are density, temperature, three components of drift velocity, and three components of heat flow.

²⁴ H. Grad, *Comm. Pure Appl. Math.* **2**, 331 (1949).

²⁵ K. Molvig, A. N. Simakov, and E. L. Vold, *Phys. Plasmas* **21**, 092709 (2014)

²⁶ Referring to Schunk’s notation, $R_{sj} = (m_s/n_j) v_{sj}\Phi_{sj}$, where m_s is the particle mass of species s , v_{sj} is the momentum transfer collision frequency between species, and Φ_{sj} is a dimensionless factor that depends on the species’ relative velocity and the details of the interparticle potential. Φ_{sj} is of order unity for subsonic relative velocity.

²⁷ Ya. B. Zel'dovich and Yu. P. Raizer, *Physics of Shock Waves and High-Temperature Hydrodynamic Phenomena*, Ch. VII §4 (Dover, 2002).

²⁸ G. Kagan and X.-Z. Tang, *Phys. Lett. A* **378**, 1531 (2014); G. Kagan and X.-Z. Tang, *Phys. Plasmas* **21**, 022708 (2014).

²⁹ As will be discussed later, there is a danger that this distinction in the behavior of $\nabla T_i/T_i$ and $\nabla P_s/P_s$ is suppressed in “clean” simulations, leading to mistaken estimates of their relative magnitudes.

³⁰ S. I. Braginskii, “Transport Processes in a Plasma”, in *Reviews of Plasma Physics*, pp. 205-311, M. A. Leontovich, ed. (Consultants Bureau, New York, 1965).

³¹ J. D. Huba, *NRL Plasma Formulary*, pp. 37-38 (Plasma Physics Division, Naval Research Laboratory, Washington D. C., 2002)

³² H. Bosch and G. M. Hale, *Nucl. Fusion* **32**, 611 (1992)

³³ G. Dimonte, *Phys. Plasmas* **7**, 2255 (2000).

³⁴ S. H. Cheung, T. A. Oliver, E. E. Prudencio, S. Prudhomme, and R. D. Moser, *Rel. Engng. System Safety* **96**, 1137 (2011).

³⁵ J. T. Oden and S. Prudhomme, *Int. J. Numer. Meth. Engng.* **87**, 262 (2011).

³⁶ We replace absolute yields such as Y_{DD} , Y_{D3He} , etc., with their base-10 logarithms in Eq. 9, and replace the corresponding absolute uncertainty σ of yield Y with the uncertainty in the base-10 logarithm of Y , i.e., $\sigma_{rel} \equiv (\sigma/Y \ln 10) \cong 0.434(\sigma/Y)$. When the observed and simulated values of observable quantity Q are not too different, so $Q \cong Q_{obs} \cong Q_{sim}$, the absolute and logarithmic forms are nearly equivalent. When Q_{obs} differs from Q_{sim} by a large amount, the logarithmic form gives a larger contribution to S_N than the absolute form, and hence a stronger penalty for the discrepancy.

³⁷ Many other more refined optimization strategies are possible. These include, for example, (1) more comprehensive sampling strategies such as Latin hypercube sampling; (2) higher order searches in which a continuous “response surface” is fitted to each of the discrete output functions $Y_{DDn,sim}(f_{dif}, f_{icnd})$, $Y_{D^3He,sim}(f_{dif}, f_{icnd})$, etc., giving a continuous approximation of $S_N(f_{dif}, f_{icnd})$ for arbitrary interpolated values of f_{dif} and f_{icnd} ; (3) nested searches of discrete subsets of input space on refined grids containing the optimum found on a coarser grid, perhaps accelerated by Newton’s Method based on the gradient of S_N ; (4) Markov-Chain Monte Carlo methods exploring input space using a random sequential algorithm. These techniques have not been pursued here, but remain for future work.

³⁸ Hydrodynamic instability and turbulent mixing are often invoked as explanations when observed yield is much smaller than clean yield in an ICF capsule implosion. In thin-shell “exploding pusher” implosions such as the ones described in this article, however, it is extremely unlikely that such hydrodynamic phenomena play a significant role. This point was made convincingly by Rosenberg *et al.*¹³, and by Rinderknecht *et al.*^{11,12} in analyzing the thin deuterated-shell capsule implosions discussed in Sec. III.E.1. In the calibration process just described, models with $l \neq 0$ were allowed during the optimization, but were not needed to find good fits to the data. We take this as further evidence that turbulent mixing is unimportant here.

³⁹ J. R. Rygg, J. A. Frenje, C. K. Li, F. H. Séguin, R. D. Petrasso, J. A. Delettrez, V. Y. Glebov, V. N. Goncharov, D. Meyerhofer, S. Regan, T. Sangster, and C. Stoeckl, *Phys. Plasmas* **13**, 052702 (2006).

⁴⁰ Nevertheless, the calculated burn-rate-weighted mean values of T_{iD^3He} and T_{iDD} often differ significantly in RIK simulations, even though the hydrodynamic code enforces a single temperature for all ion species. This is because the fusion reactivities $\langle \sigma v \rangle_{D^3He}$ and $\langle \sigma v \rangle_{DD}$ have different temperature dependences and are modified by differing amounts by the Molvig-

Albright reactivity-reduction model, and because the fractional compositions of D and ^3He vary in space and time owing to differential ion transport. These effects cause the space and time dependence of the two reaction rates, which are the weighting functions determining $T_{iD^3\text{He}}$ and T_{iDD} , to be quite different. The presence of large temperature gradients in the burning fuel then leads to quite different values of $T_{iD^3\text{He}}$ and T_{iDD} .